



저작자표시-비영리-동일조건변경허락 2.0 대한민국

이용자는 아래의 조건을 따르는 경우에 한하여 자유롭게

- 이 저작물을 복제, 배포, 전송, 전시, 공연 및 방송할 수 있습니다.
- 이차적 저작물을 작성할 수 있습니다.

다음과 같은 조건을 따라야 합니다:



저작자표시. 귀하는 원저작자를 표시하여야 합니다.



비영리. 귀하는 이 저작물을 영리 목적으로 이용할 수 없습니다.



동일조건변경허락. 귀하가 이 저작물을 개작, 변형 또는 가공했을 경우에는, 이 저작물과 동일한 이용허락조건하에서만 배포할 수 있습니다.

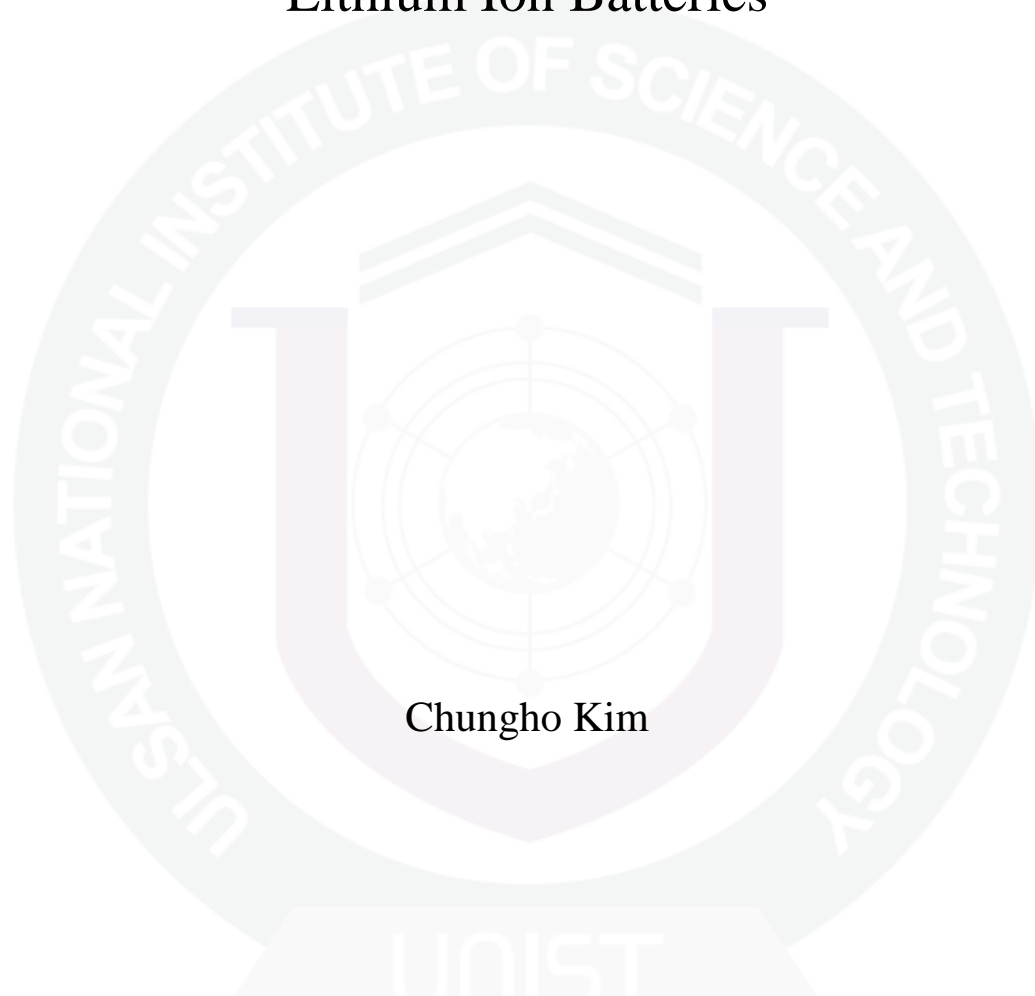
- 귀하는, 이 저작물의 재이용이나 배포의 경우, 이 저작물에 적용된 이용허락조건을 명확하게 나타내어야 합니다.
- 저작권자로부터 별도의 허가를 받으면 이러한 조건들은 적용되지 않습니다.

저작권법에 따른 이용자의 권리는 위의 내용에 의하여 영향을 받지 않습니다.

이것은 [이용허락규약\(Legal Code\)](#)을 이해하기 쉽게 요약한 것입니다.

[Disclaimer](#)

Synthesis of Nanostructured Materials and their
Electrochemical Study as Anode Materials of
Lithium Ion Batteries



Chungho Kim

Department of Chemical Engineering
Graduate School of UNIST

2013

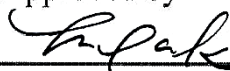
Synthesis of Nanostructured Materials and their Electrochemical Study as Anode Materials of Lithium Ion Batteries

A thesis
submitted to the Graduate School of UNIST
in partial fulfillment of the
requirements for the degree of
Master of Science

Chungho Kim

12. 18. 2013 of Submission

Approved by



Major Advisor

Jongnam Park

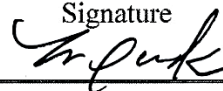
Synthesis of Nanostructured Materials and their Electrochemical Study as Anode Materials of Lithium Ion Batteries

Chungho Kim

This certifies that the thesis of Chungho Kim is approved.

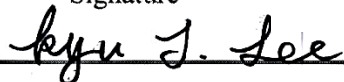
12. 18. 2013 of Submission

Signature



Thesis supervisor: Jongnam Park

Signature



Name of Thesis Committee Member: Kyu Tae Lee

Signature



Name of Thesis Committee Member: Yoon Seok Jung

Abstract

Nanostructured materials have been receiving increasing attention in recent years because of the interesting mechanical, optical and electrical properties that such materials offer. In particular, the development of nanostructured electrodes for lithium ion batteries has attracted the interest of a number of researchers due to the advantages offered in terms of new reaction mechanisms that are not possible with bulk materials, better buffering of volume expansion and shorter pathways for Li^+ ion and electron transport. In field of current lithium ion batteries, it is necessary to use new negative electrode materials which have high capacity, low cost and environmental benignity. In tandem with above phenomenon, development of new nanostructured electrode materials for lithium ion batteries also work up the excitement of researchers due to many advantages. Successful strategies were that one method is surface coating for increase conductivity or reduce side reaction, aggregation of the nanoparticles and another method is controlling of nanoparticle's morphology for enhance their specific surface area so that the kinetics would be improved and serve buffer space of the active material volume expansion. Although various methods have been previously developed for fabricating a self-assembled structure, these approaches tend to be based on either inert conditions or to rely on complex high temperature, high pressure process. And some approach (crystalline conversion reaction materials replace to amorphous conversion reaction materials) is not clearly veil the effect. To overcome these problems, new facile methods of anode materials have developed and the understanding of new anode materials synthesis mechanism and the improvement of lithium ion batteries were performed. For example, I introduce a facile method to prepare for the Ni_2P nanostructures with controlled crystallinity and morphology and unveil a pure difference between crystalline and amorphous Ni_2P as anode material for rechargeable lithium ion batteries. Furthermore, i developed Graphene Oxide Assisted Synthesis of Self-assembled Zinc Oxide for Lithium-Ion-Battery anode without hash condition.

Blank page

Table of Contents

Title page -----	I
Signature Page -----	III
Abstract -----	IV
Table of Contents -----	VI
List of Figures -----	VIII
List of Tables -----	XI
Nomenclature -----	XII

CHAPTER 1: Introduction and Motivation

1.1 Introduction and Motivation-----	1
1.2 Lithium ion batteries -----	6
1.3 Electrode materials -----	9
1.3.1 Insertion electrode materials -----	9
1.3.2 Alloying electrode materials -----	12
1.3.3 Conversion electrode materials -----	12
1.4 Thesis Overview -----	14
1.5 References -----	14

CHAPTER 2: A Facile Method to Prepare for the Ni₂P Nanostructures with Controlled Crystallinity and Morphology as Anode Materials of Lithium Ion Batteries

2.1 Introduction -----	18
2.2 Experimental -----	22
2.2.1 Materials -----	22
2.2.2 Synthetic method -----	22
2.3 Result and Discussion -----	23
2.4 Conclusions -----	38
2.5 Reference -----	39

CHAPTER 3: Graphene Oxide Assisted Synthesis of Self-assembled Zinc Oxide for LIB

3.1 Introduction -----	41
3.2 Experimental -----	42
3.2.1 Materials -----	42

3.2.2 Synthetic method -----	42
3.3 Result and Discussion -----	43
3.3.1 The synthetic mechanism of SAZO@GO & Temperature tendency -----	43
3.3.2 Moisture effect -----	48
3.3.3 Controlling of SAZO@rGO ratio -----	52
3.3.4 Improving of conductivity -----	53
3.3.5 Electrochemical measurement -----	56
3.4 Conclusions -----	61
3.5 Reference -----	62

List of figures

- Figure 1.1: Ratio of Surface atoms to interior atoms
- Figure 1.2: Schematic illustration of practical application fields of nanostructured materials
- Figure 1.3: Schematic illustration of examples of practical application
- Figure 1.4: Graph of Dubai crude oil price
- Figure 1.5: Effect of surface coating
- Figure 1.6: Schematic illustration of (a) a redox reaction, (b) a primary battery and (c) a secondary battery.
- Figure 1.7: The operating voltages, redox couples and overall reactions involved in the main rechargeable battery chemistries.
- Figure 1.8: Schematic illustration of a lithium-ion battery ($\text{LiCoO}_2/\text{graphite}$)
- Figure 1.9: Schematic illustration of the three types reaction mechanisms; Black circles: voids in the crystal structure, blue circles: metal, yellow circles: lithium.
- Figure 1.10: The formation of a monoclinic phase with nonuniform lattice constant expansion (2.6%) in bare LiCoO_2 during charging (Li deintercalation)
- Figure 1.11: a) DSC scans of anode graphite and cathode Li_xCoO_2 after 100% charging and b) accelerating rate calorimetry of various cathodes after 100% charging.
- Figure 1.12 Crystal structures and capacities of Group IV elements; C (LiC_6), Si ($\text{Li}_{4.4}\text{Si}$), Ge ($\text{Li}_{4.25}\text{Ge}$), Sn ($\text{Li}_{4.25}\text{Sn}$), and Pb ($\text{Li}_{4.25}\text{Pb}$).
- Figure 2.1: Typical voltage vs. composition profile of the conversion reaction materials
- Figure 2.2: specific gravimetric capacities of different compounds that react with lithium through a conversion reaction
- Figure 2.3: Schematic illustration of the formation of nickel phosphides
- Figure 2.4: High power-XRD data of (a) amorphous Ni_2P nanoparticle clusters (b) crystalline Ni_2P nanoparticle clusters (c) self-assembled Ni_2P nanoparticle clusters.
- Figure 2.5: Normal TEM image of (a), (b) crystalline Ni_2P nanoparticle clusters; (c), (d) amorphous Ni_2P nanoparticle clusters; (f), (g) self-assembled Ni_2P nanoparticle clusters; EDS data of (e) amorphous Ni_2P nanoparticle clusters
- Figure 2.6: SEM image of self-assembled Ni_2P nanoparticle cluster by concentration of Ni-TOP solution; (a) 0.1 M (b) 0.25 M (c) 0.5 M
- Figure 2.7: Cyclic performance of Ni_2P nanoparticle cluster electrodes at 0.5 C
- Figure 2.8: Charge and discharge capacities of Ni_2P nanoparticle cluster electrodes at 0.5 C
- Figure 2.9: GITT curves of amorphous and crystalline Ni_2P electrodes in first cycle.
- Figure 2.10: GITT curve of (a) amorphous Ni_2P electrode (b) crystalline Ni_2P electrode

Figure 2.11: Voltage difference from GITT curve between close circuit voltage and open circuit voltage on 1st discharge and charge process

Figure 2.12: (a) 1st cycle and 2nd discharge curve of nickel phosphide electrodes. (b) Voltage hysteresis curve between 1st charge and 2nd discharge profile.

Figure 2.13: (a), (b) images of 2016 coin type half-cell after fully lithiation (c) Voltage profiles (solid line) of Ni₂P nanoparticles clusters electrodes and the corresponding electrode thickness change (bar) during lithiation and delithiation.

Figure 2.14: CV curves of amorphous Ni₂P and crystalline Ni₂P electrodes for (a) the first cycle and (b) the second and third cycles with a scan rate of 0.2 mV s⁻¹ from 0.02 to 3.0 V.

Figure 3.1: Illustration depicting the preparation of self-assembled ZnO

Figure 3.2: TEM images of ZnO/GO synthesized at temperatures of (A) 125 °C (B) 95 °C (C) 85 °C (D) 45 °C

Figure 3.3: SEM images of ZnO/GO with varying temperature (A) 125 °C (B) 95 °C (C) 85 °C (D) 45 °C

Figure 3.4: XRD patterns of ZnO/rGO with various temperatures of synthesis A) 125 °C (B) 95 °C (C) 85 °C (D) 45 °C

Figure 3.5: TEM images of (a) ZnO nanoparticle clusters (b) doughnut-like ZnO

Figure 3.6: Time series of TEM image of ZnO/rGO

Figure 3.7: TEM images and picture of result product after ZnO synthesis at the inert condition

Figure 3.8: TEM images of ZnO/GO at 85 °C with various cosolvent ratios of DMF/DI water = (A) 250 : 0, (B) 240 : 10, (C) 225 : 25, and (D) 200:50

Figure 3.9: SEM images of ZnO/rGO with varying cosolvent ratios DMF : DI water = (A) 250 : 0 (B) 240: 10 (C) 225:25 (D) 200 : 50

Figure 3.10: XRD patterns of ZnO/rGO with varying cosolvent ratios DMF : DI water = (A) 250 : 0 (B) 240: 10 (C) 225:25 (D) 200 : 50

Figure 3.11: (a) TGA curves of synthesis temperature dependent SAZO@GO; red line 125 °C, black line 95 °C. (b) XRD pattern of self-assembled ZnO and doughnut-like ZnO samples. (c) Raman spectra of GO and self-assembled ZnO with GO. (d) Electronic conductivity of SAZO@GO and SAZO@rGO.

Figure 3.12: TGA curve of GO and SAZO@GO

Figure 3.13: SEM images of SAZO@rGO before and after calcination under air atmosphere at 500 °C

Figure 3.14(a) Cyclic voltammograms of the SAZO@rGO electrode at a scanning rate of 0.2 mV s⁻¹. (b) Discharge-charge curves for SAZO@rGO. (c) Cycling performance of ZnO electrodes at a current density of 100 mA g⁻¹. (d) Rate performance of ZnO electrodes

Figure 3.15 Cycling performance of ZnO electrodes at a current density of 500 mA g⁻¹.

Figure 3.16 SEM images of SAZO@rGO and DLZO@rGO electrodes before and after cycling; SEM images of (a, b) bare SAZO@rGO electrode and (e, f) bare DLZO@rGO electrode. SEM images of (c, d) SAZO@rGO electrode and (g, h) bare DLZO@rGO electrode after 100cycles in condition of current density 500 mA g^{-1} .

List of tables

Table 1. 1 Advantages and disadvantages of nanostructured materials for lithium ion batteries

Table 1. 2 The voltage, theoretical specific energy values of rechargeable batteries.

Table 1. 3 The table of the theoretical specific capacity, charge density, volume change and onset potential of various anode materials.

Nomenclature

SEM	Scanning Electron Microscope
EDS	Energy Dispersive Spectroscopy
TEM	Transmission Electron Microscope
XRD	X-ray diffraction analysis
ORR	Oxygen reduction reaction
OER	Oxygen evolution reaction
CV	Cyclic voltammetry
SEI	Solid electrolyte interface

Chapter 1

Introduction and Motivation

1.1 Introduction and motivation

Nanostructured materials have been receiving especial attentions since the early 2000s due to their interesting magnetic, optical, electronic, chemical, and catalytic properties.¹ A lot of researchers had been trying to unveil origin of their novel properties and looking for their practical applications. Their unique properties are contributed to high surface to volume ratio, quantum confinement effect and new reaction not possible with bulk materials.^{1a} For example, a dramatic increasing in the ratio of surface atoms to interior atoms occurs when the size of bulk is reduced to nanometer scale (figure 1.1). It means that the physical and chemical properties are changed. And strong quantum confinement is observed for many semiconductor nanocrystals because the size of a semiconductor crystal is reduced below the material's bulk Bohr exciton radius, the electronic structure evolves from a set of bands of continuum states to a set of discrete atomic-like states.

Nowadays, the researches of nanostructured materials revolve around technological applications of its by conflation with information technology (IT), energy technology (ET), bio technology (BT) and so on for overcome their traditional problems. For example, nanostructured materials (especially monodisperse nanocrystals) are crucial for the multi-terabit magnetic storage media^{1b}, they are also becoming increasingly important for electrochemical energy storage include energy storage system (ESS), lithium ion batteries for electrical vehicles (EVs).^{1a, 2} And some metal nanoparticles have been extensively researched as catalysts for Suzuki coupling reactions³, ORR and OER.⁴

Specially, research of electrochemical energy storage systems are becoming more important on use of new renewable energy generation such as solar, wind and tidal energy due to the growing concern over global warming, air pollution and crucial oil price increasing. In tandem with above phenomenon, development of nanostructured electrode materials for lithium ion batteries also work up the excitement of researchers due to many advantages include new reaction mechanisms not possible with bulk materials, short pathways of Li^+ ion and electronic transport, better buffering of volume expansion and etc.^{1a, 2b} Above advantages have been becoming to chance for overcome current lithium ion battery's limitation. This being so, many people are trying to research a nanostructured electrodes.

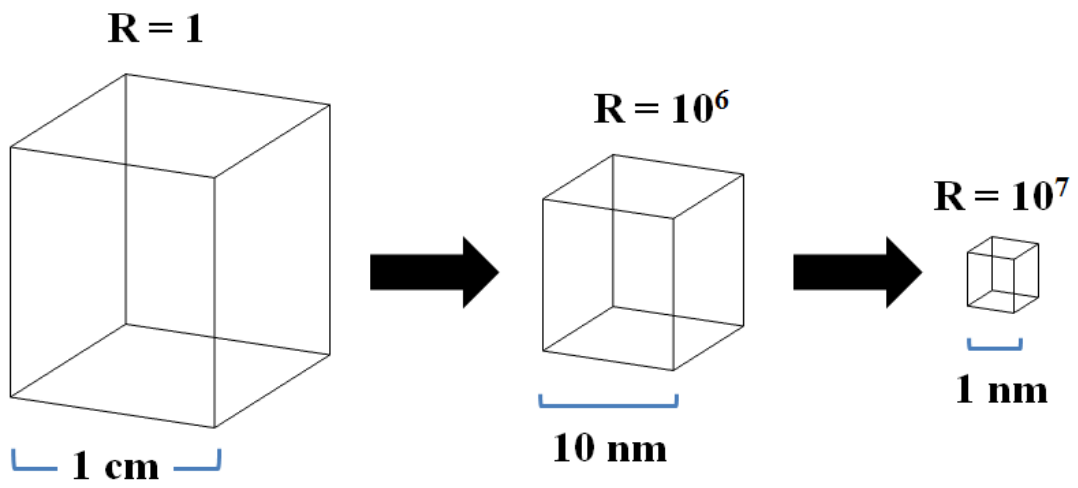


Figure 1.1 Ratio of surface atoms to interior atoms

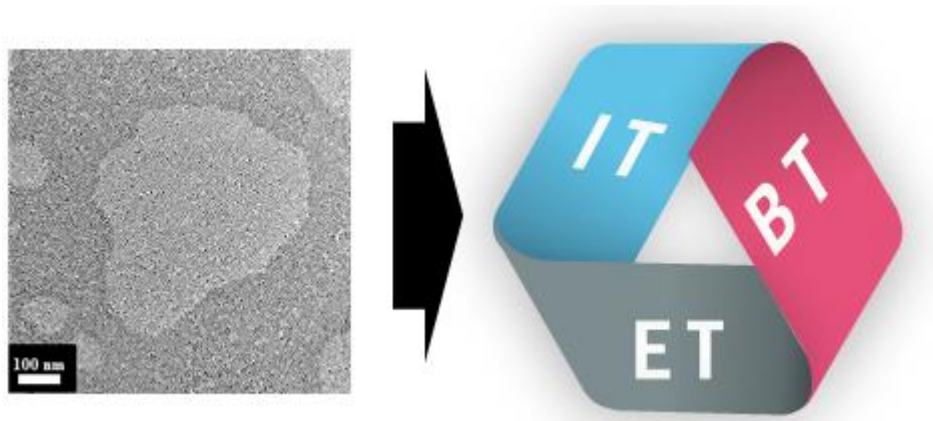


Figure 1.2 Schematic illustration of practical application fields of nanostructured materials

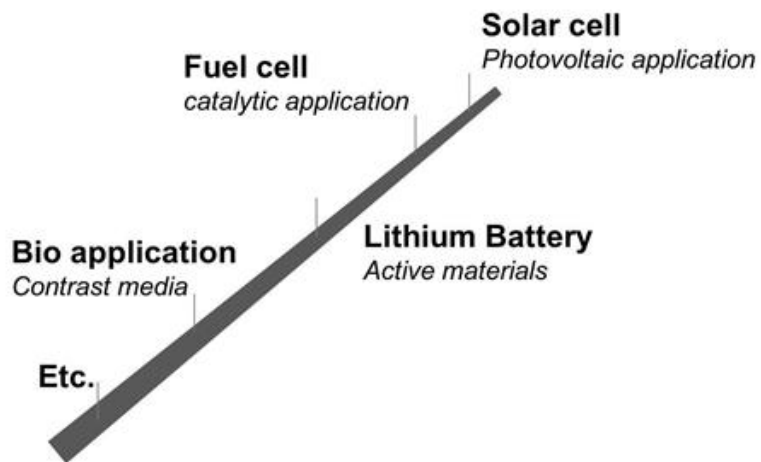


Figure 1.3 Schematic illustration of examples of practical application

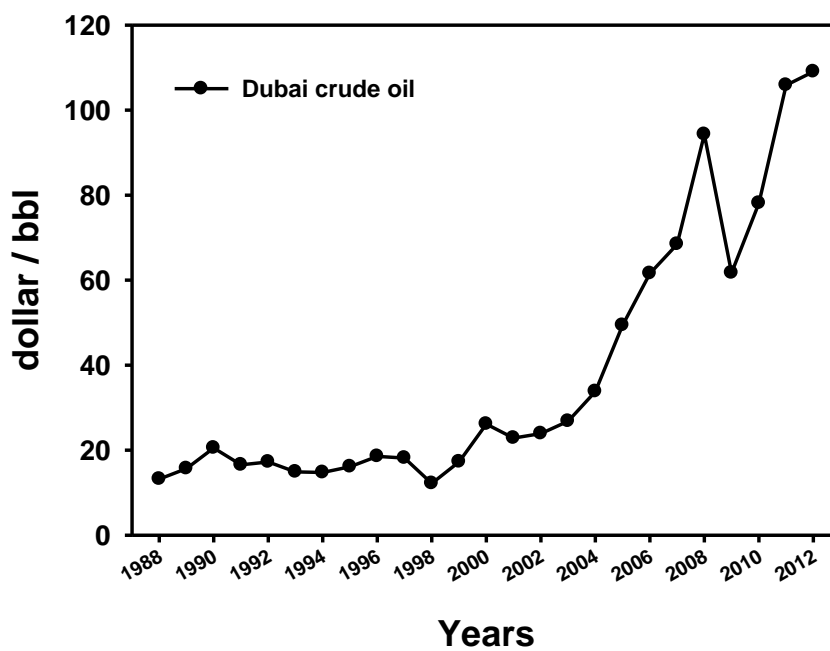


Figure 1.4 Graph of Dubai crude oil price

Unfortunately, notwithstanding these major advantages, nanostructured materials have many drawbacks to use electrodes of lithium ion batteries. A few critical problems had not being still solved include inferior packing of particles leading to lower volumetric energy densities, an increase of side reaction in undesirable electrode/electrolyte reactions, self-discharge, poor cycling and calendar life (table 1.1).^{2b}

Therefore, many research approaches of nanostructured materials as electrodes of lithium ion batteries are mostly on method to overcome their problems. Successful strategies to triumph over these problems were that one method is surface coating for increase conductivity or reduce side reaction, aggregation of the nanoparticles.⁵ For example, carbon coating has been a major approach, since the carbon moiety may increase conductivity, reduce aggregation of the nanoparticles.^{5a} Furthermore, a carbon coating on the surface of nanoparticles can decrease the undesirable reactions at the interface between active materials and electrolyte. Moreover, carbon coating can improve the low conductivity of active materials.^{5a,6} Second approach is morphology control of nanoparticle for maximize nanoparticle's benefits.⁷ Controlling of nanoparticle's morphology could enhance the kinetics and serve buffer space of the active material volume expansion with the result that specific surface area is enhanced.⁸ Therefore, well controlled structure would lead to a better cycle ability. Main strategy is that the morphology of active material makes hollow structure or nanowires (nanofibers, nanotubes).⁸⁻⁹ These approaches lead to the stable cycle performance and higher rate capability for active materials than other structures.

However, these approaches include inert condition or high temperature, high pressure and complex process.¹⁰ Moreover, some convenient methods are also needed additional steps for a surface coating after synthesis of active materials.¹¹ Therefore, other methods include new synthesis or approaches to overcome their problems are needed.

In this dissertation, new facile methods of new anode materials have developed and the understanding of new anode materials synthesis mechanism and the improvement of lithium ion batteries were performed.

Advantages	Disadvantages
1. New reaction mechanisms not possible with bulk materials	1. Complex synthesis and control of nanoparticles
2. Short diffusion length for lithium ion transport within the particles.	2. Side reactions on surface between the electrolyte and electrodes
3. Enhance an electron transport by nanoparticles	3. Low tap-density compared with micrometer-sized particles
4. A change of electrode potential in case of very small particles	
5. The range of composition over which solid solutions exist is often more extensive for nanoparticles, and the strain associated with intercalation is often better accommodated.	

Table 1.1 Advantages and disadvantages of nanostructured materials for lithium ion batteries.

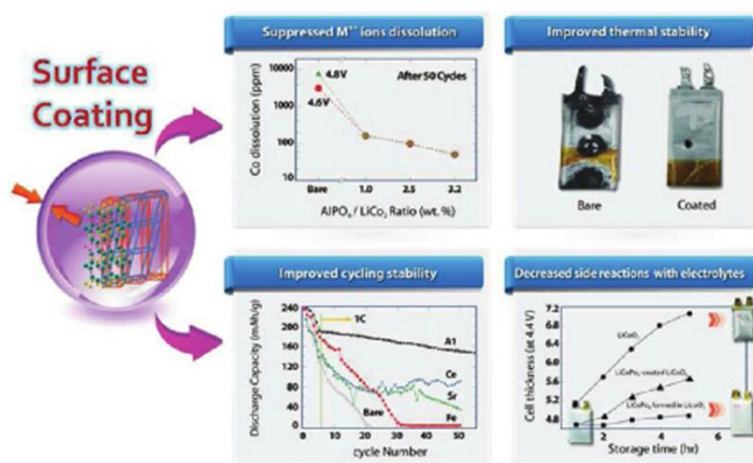


Figure 1.5 Effect of surface coating.^{5c}

1.2 Lithium ion batteries

Energy storage devices are also gradually to be important with new energy sources which are based on eco-friendly and abundant resources like solar radiation, wind and waves due to global warming and crucial oil price increasing.¹²

When brief looking into batteries history, some ancient societies may have first developed chemical devices of the kind (Baghdad Battery was developed at probably 200 BC), the batteries in modern times is ascribed to Alessandro Volta in the beginning of the 19th century. Since Volta's works, there are two innovative advance of batteries technology. First, secondary batteries had developed over primary batteries. Secondary batteries are called rechargeable batteries, while primary batteries are non-rechargeable batteries (figure 1.6). Second, operation voltages shoot up to over 3 V (figure 1.7). Especially, lithium ion batteries continuously have been developing to improve of annual average 10% their energy densities.

Currently, secondary lithium ion batteries have been the focus of promising power source for not only cell phones, laptops but EVs, ESS in comparison with other rechargeable batteries like lead-acid battery, Ni-Cd battery and etc. (except for Na/S, ZEBRA batteries, table 1.2).

Commercial lithium ion batteries utilize layered structure lithium metal oxide or olivine structure lithium metal phosphate as a cathode and graphite as an anode where lithium ions intercalate into or de-intercalate between two electrodes, which is called "rocking-chair battery" (figure 1.8). Famous commercial lithium ion batteries are consisted of LiCoO_2 cathode and carbon anode, separator with an electrolyte. These commercial lithium ion batteries have been widely applied in current consumer electronic devices for not only cell phones but also portable electronic devices. This well-known system of reversible chemistry had a concept of "host-guest" chemistry by brilliant scientist Whittingham and the significant improvements by Goodenough et al.

Since the commercialization of LiCoO_2 /Carbon system, the demands of lithium ion batteries have been extending to transportation markets, particularly for full scale electrical vehicles (EV), and energy storage system markets. However, current system has limitation of energy below 250Wh kg^{-1} and 800Wh L^{-1} . Therefore, it is necessary to use new positive and negative materials which have high capacity, low cost, environmental benignity to improve the current lithium ion batteries performance.

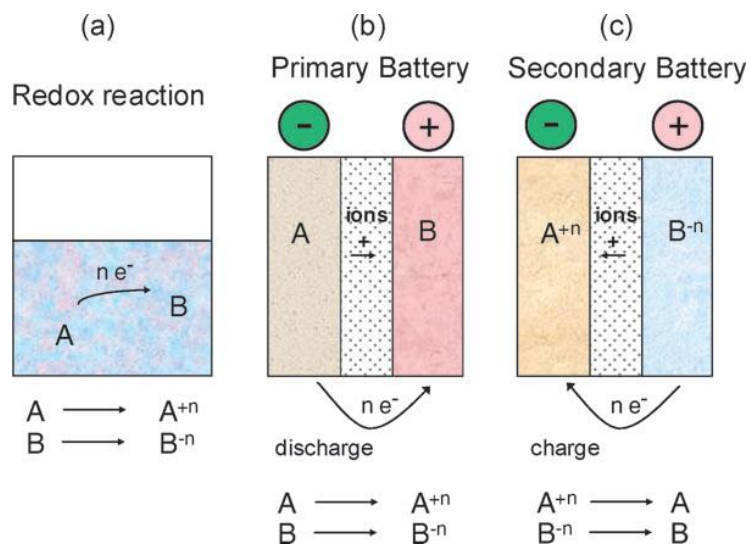


Figure 1.6 Schematic illustration of (a) a redox reaction, (b) a primary battery and (c) a secondary battery.^{12d}

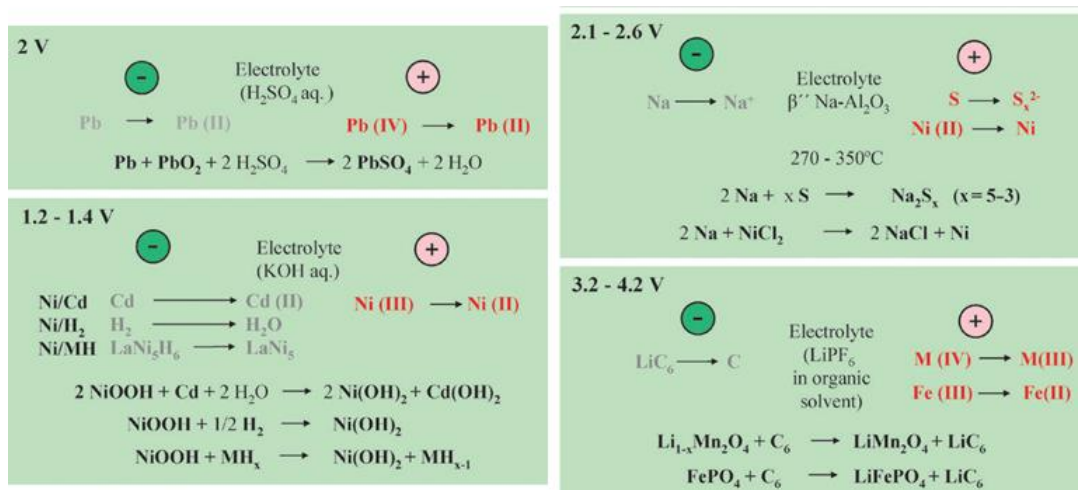


Figure 1.7 The operating voltages, redox couples and overall reactions involved in the main rechargeable battery chemistries.^{12d}

Battery chemistry	Type	Voltage/V	Theoretical specific energy/W h kg ⁻¹	Practical specific energy/W h kg ⁻¹	Practical energy density/W h dm ⁻³
Pb/acid	Secondary	2.1	252	35	70
Ni/Cd	Secondary	1.3	244	35	100
Ni/MH	Secondary	1.3	240	75	240
Na/S	Secondary	2.1	792	170	345
Na/NiCl ₂	Secondary	2.6	787	115	190
Lithium ion	Secondary	4.1	410	150	400

Table 1.2 The voltage, theoretical specific energy values (considering only the mass of the active materials in the electrodes), values achieved in practice and energy densities for the major battery systems (there is a large range of values for lithium-ion batteries owing to the great variety of available electrode materials, both for the positive and negative electrodes).^{12d}

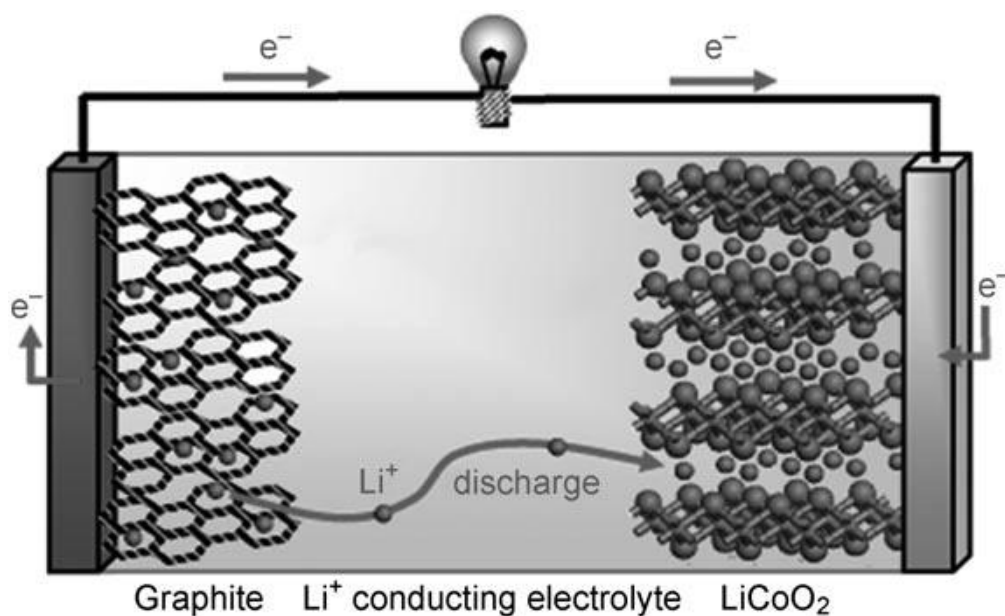


Figure 1.8 Schematic illustration of a lithium-ion battery (LiCoO₂/graphite).^{1a}

1.3 Electrode materials

The kinds of electrode materials can classify three types on the reaction process, insertion (or intercalation), alloying and conversion materials (figure 1.9). The current electrode materials in commercial batteries are based on topotactic reversible intercalation of lithium ions without major structural changes include LiCoO_2 , graphite. However, the markets of lithium ion batteries are growing and the demand of consumers get increasing for EV and ESS. Therefore, people are trying to find new electrode materials for not only improve their performance and safety, but reduce a cost. In current commercial lithium ion batteries, LiCoO_2 is very stable and good electrode materials. However, its useful capacity is close to just 150 mAh g^{-1} which is almost half of their theoretical capacity. Because Li_xCoO_2 convert original hexagonal phase to monoclinic phase with c-axis expansion of up to 2.6% at over $x = 0.5$ and the structure are collapse (figure 1.10).¹³ And cobalt has toxicity and it is expensive. Furthermore, graphite is very good anode electrode materials but it has critical limitation of low theoretical capacities $\sim 274 \text{ mAh g}^{-1}$. To overcome current limitation and fill a market demands, people trying to research three types of electrode materials.

1.3.1 Insertion electrode materials

Insertion electrode materials are doing reversible intercalation reaction with lithium ions without major structural changes. Currently, various insertion electrode materials have developed and developing for replace cathode LiCoO_2 , anode graphite. In particular, the researches of insertion materials are mainly cathode materials. For example, LiFePO_4 at the positive electrode material have intensely researched for replace LiCoO_2 . The LiFePO_4 has an olivine structure.¹⁴ The reasons of replacement LiCoO_2 to LiFePO_4 are safety and cost. As you already know, the cobalt is very expensive and it will become more costly due to rising of demand. However, iron is one of abundant metal and it is more cheaper than cobalt. And LiCoO_2 is one of very dangerous electrodes due to triggering mechanism which induces thermal runaway. In safety problems of lithium ion batteries, cathode materials (extremely LiCoO_2) are at the center of the controversy. The quantity of heat generation from electrode materials show that LiFePO_4 is very stable and safe compared with other cathode electrode materials (figure 1.11).¹⁵ The other candidate electrodes like layered LiMO_2 ($M = \text{Ni, Mn, Co}$), spinel LiMnO_4 , olivine LiMPO_4 , over lithiated layered oxides (OLO) cathode materials are also developed as almost same reason (safety, cost, capacities).

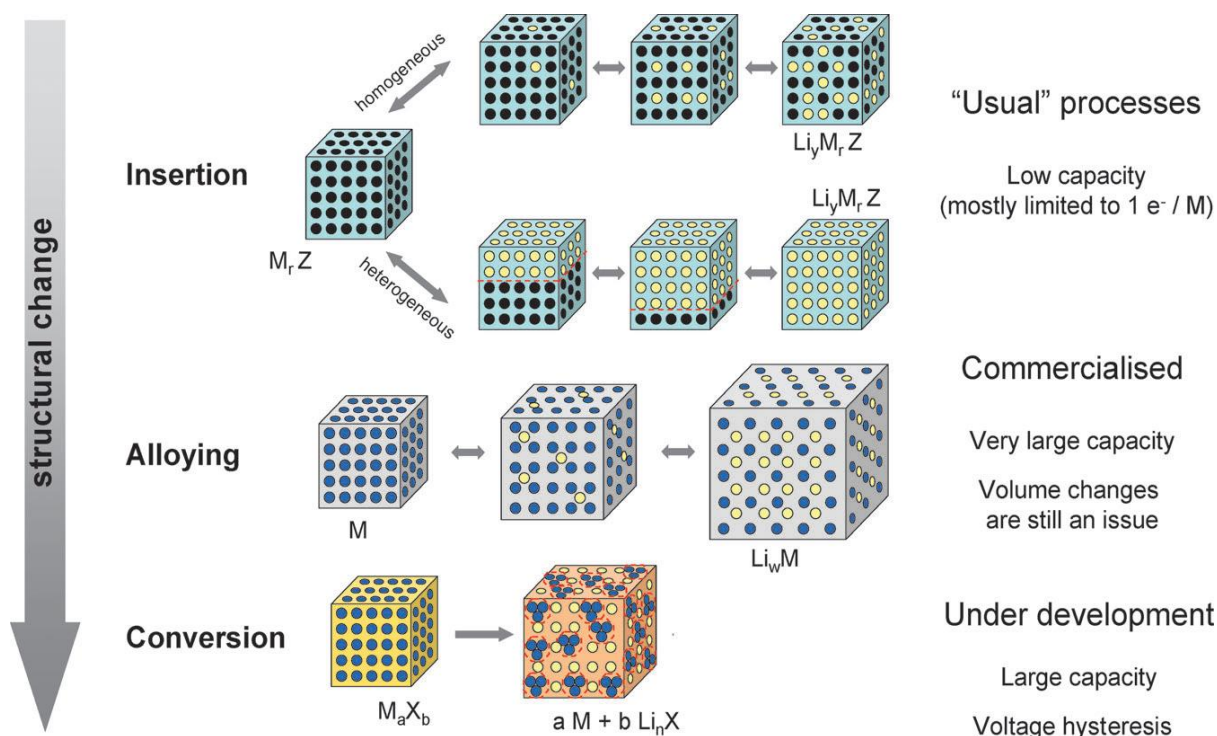


Figure 1.9 Schematic illustration of the three types reaction mechanisms; Black circles: voids in the crystal structure, blue circles: metal, yellow circles: lithium.^{12d}

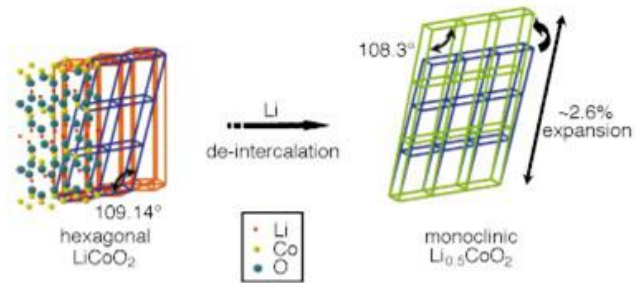


Figure 1.10 The formation of a monoclinic phase with nonuniform lattice constant expansion (2.6%) in bare LiCoO_2 during charging (Li deintercalation)¹³

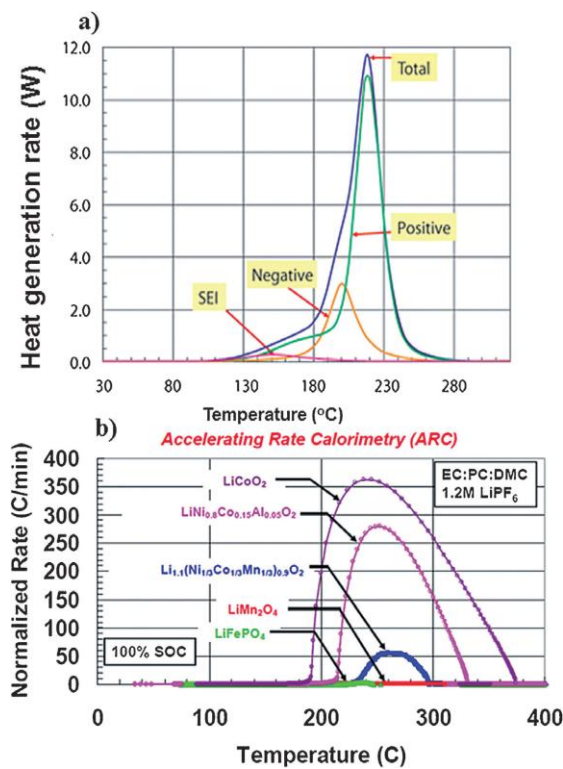


Figure 1.11 a) DSC scans of anode graphite and cathode Li_xCoO_2 after 100% charging and b) accelerating rate calorimetry of various cathodes after 100% charging.¹⁵

1.3.2 Alloying electrode materials

Alloying electrode materials have developed and developing for replace mainly current anode graphite which has low theoretical energy density (372 mAh g^{-1}) and safety issues. They are known for their good safety characteristics and high specific capacities compared with insertion electrode materials (table 1.3). Theoretical specific capacity (mAh g^{-1}) of alloying electrode materials has 2~20 times higher than that of $\text{Li}_4\text{Ti}_5\text{O}_{12}$ or graphite and the charge densities (mAh cm^{-1}) of alloy anodes are still 2~5 times higher than that of graphite and $\text{Li}_4\text{Ti}_5\text{O}_{12}$.¹⁶ It is a big merit to improve battery performance as anodes of lithium ion batteries. Moreover, operating potentials versus lithium are more suitable for apply anodes of lithium ion batteries than insertion materials. For example, silicon which is most candidate anode electrode materials has a suitable potential (vs. Li) of 0.4 V compared with that of 0.05 V of graphite and that of 1.5 V of $\text{Li}_4\text{Ti}_5\text{O}_{12}$. Graphite has too low potential and $\text{Li}_4\text{Ti}_5\text{O}_{12}$ has too high potential. This suitable potential make reduce the safety issue of lithium deposition in graphite anode and avoids the energy penalty by high potential of $\text{Li}_4\text{Ti}_5\text{O}_{12}$.¹⁶

Hence, alloying electrode materials is being studied with great interest but the large volume change which cause the rapid capacity fading during cycling is still hot issue because it is big obstacle their applicability to practical lithium ion batteries.¹⁶ To overcome their critical problems, various approaches are performed include multiphase composites¹⁷, particle size control¹⁸, intermetallic, thin film and amorphous alloys, operating voltage control.¹⁶

1.3.3 Conversion electrode materials

Conversion reaction can be expressed that active electrode is consumed by Li ion and converted to embedded nanometer scale metal in lithium-anion matrix. Conversion electrode materials have great advantages. For example, it has a high theoretical capacity due to transfer of more than one electron per 3D metal on redox cycle. Good electronic conductivity from Li-X matrix ($X = \text{O, F, N, S, P}$) and short diffusion distance from metal nanocomposite are also benefit.¹⁹

However, conversion electrode materials are still under development due to many problems include large volume change, low electrical conductivity, poor kinetics, large voltage hysteresis, low ICE.¹⁹ Therefore, the research of kinetic improvements and enhancement of their capacity retention in conversion reactions are pretty performed like particle size control, surface coating, thin film and new nanostructured design.^{19b}

Materials	Li	C	Li ₄ Ti ₅ O ₁₂	Si	Sn	Sb	Al	Mg	Bi
Lithiated phase	Li	LiC ₆	Li ₇ Ti ₅ O ₁₂	Li _{4,4} Si	Li _{4,4} Sn	Li ₃ Sb	LiAl	Li ₃ Mg	Li ₃ Bi
Theoretical specific capacity (mAh g ⁻¹)	3863	372	175	4200	994	660	993	3350	385
Theoretical charge density (mAh cm ⁻³)	2047	837	613	786	7246	4422	2681	4355	3765
Volume change (%)	100	12	1	320	260	200	96	100	215
Potential vs. Li (~V)	0	0.05	1.6	0.4	0.6	0.9	0.3	0.1	0.08

Table 1.3 The table of the theoretical specific capacity, charge density, volume change and onset potential of various anode materials (charge densities were calculated using the density of pristine metal).¹⁶

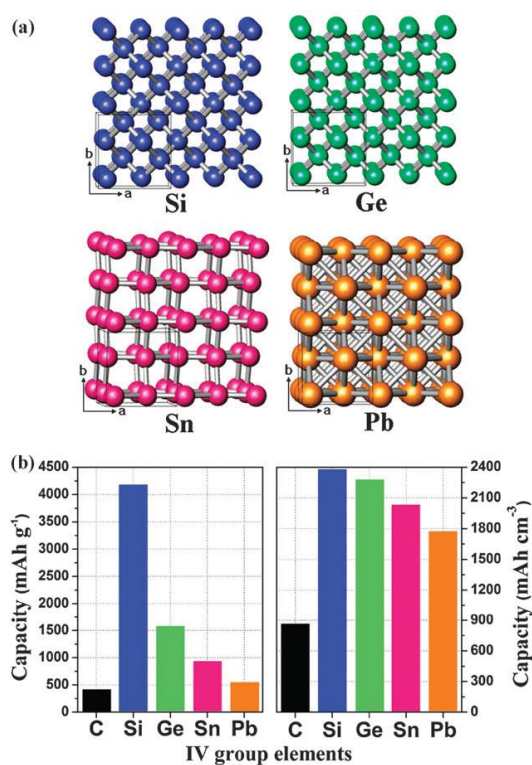


Figure 1.12 Crystal structures and capacities of Group IV elements; C (LiC₆), Si (Li_{4,4}Si), Ge (Li_{4,25}Ge), Sn (Li_{4,25}Sn), and Pb (Li_{4,25}Pb).²⁰

1.3 Thesis Overview

This thesis presents the synthesis and application of several nanostructured materials. Chapter 2 describes the preparation of 3 types nickel phosphides by using facile hot injection method and electrochemical analysis of them as an anode for unveil pure difference on conversion reaction. Chapter 3 reveals a facile reduced graphene oxide assisted synthesis of a hierarchical self-assembled zinc oxide. And hierarchical self-assembled structure could not only serve short pathways of Li^+ ion and electronic transport by nanoparticles, but also reduce side reactions on the surface between electrodes and electrolyte

1.4 References

1. (a) Bruce, P. G.; Scrosati, B.; Tarascon, J. M., Nanomaterials for rechargeable lithium batteries. *Angewandte Chemie* 2008, *47* (16), 2930-46; (b) Park, J.; An, K.; Hwang, Y.; Park, J. G.; Noh, H. J.; Kim, J. Y.; Park, J. H.; Hwang, N. M.; Hyeon, T., Ultra-large-scale syntheses of monodisperse nanocrystals. *Nature materials* 2004, *3* (12), 891-5; (c) Ovid'ko, I. A., Materials science. Deformation of nanostructures. *Science* 2002, *295* (5564), 2386.
2. (a) Lee, K. T.; Cho, J., Roles of nanosize in lithium reactive nanomaterials for lithium ion batteries. *Nano Today* 2011, *6*, 28-41; (b) Arico, A. S.; Bruce, P.; Scrosati, B.; Tarascon, J. M.; van Schalkwijk, W., Nanostructured materials for advanced energy conversion and storage devices. *Nature materials* 2005, *4* (5), 366-77; (c) Naichao Li; Charles R. Martin; Scrosati, B., Nanomaterial-based Li-ion battery electrodes. *Journal of Power Sources* 2001, *97-98*, 240-243.
3. Choi, H. R.; Woo, H.; Jang, S.; Cheon, J. Y.; Kim, C.; Park, J.; Park, K. H.; Joo, S. H., Ordered Mesoporous Carbon Supported Colloidal Pd Nanoparticle Based Model Catalysts for Suzuki Coupling Reactions: Impact of Organic Capping Agents. *ChemCatChem* 2012, *4*, 1587-1594.
4. (a) Cheng, F.; Chen, J., Metal-air batteries: from oxygen reduction electrochemistry to cathode catalysts. *Chemical Society reviews* 2012, *41* (6), 2172-92; (b) Suntivich, J.; Gasteiger, H. A.; Yabuuchi, N.; Nakanishi, H.; Goodenough, J. B.; Shao-Horn, Y., Design principles for oxygen-reduction activity on perovskite oxide catalysts for fuel cells and metal-air batteries. *Nature chemistry* 2011, *3* (7), 546-50.
5. (a) Jang, B.; Park, M.; Chae, O. B.; Park, S.; Kim, Y.; Oh, S. M.; Piao, Y.; Hyeon, T., Direct Synthesis of Self-Assembled Ferrite/Carbon Hybrid Nanosheets for High Performance Lithium-Ion Battery Anodes. *Journal of the American Chemical Society* 2012, *134*, 15010-15015; (b) Fei, L.; Lin, Q.; Yuan, B.; Chen, G.; Xie, P.; Li, Y.; Xu, Y.; Deng, S.; Smirnov, S.; Luo, H., Reduced graphene oxide wrapped FeS nanocomposite for lithium-ion battery anode with improved performance. *ACS applied materials & interfaces* 2013, *5* (11), 5330-5; (c) Lee, K. T.; Jeong, S.; Cho, J., Roles of Surface Chemistry on Safety and Electrochemistry in Lithium Ion Batteries. *Accounts of chemical research* 2012.
6. Li, B.; Cao, H.; Shao, J.; Qu, M., Enhanced anode performances of the Fe₃O₄-carbon-rGO three dimensional composite in lithium ion batteries. *Chemical communications* 2011, *47* (37), 10374-6.
7. Lu, Y.; Tu, J.-P.; Xiong, Q.-Q.; Qiao, Y.-Q.; Wang, X.-L.; Gao, C.-D.; Ma, S. X., Synthesis of dinickel phosphide (Ni₂P) for fast lithium-ion transportation: a new class of nanowires with exceptionally improved electrochemical performance as a negative electrode. *RSC Adv.* 2012, *2*, 3430-3436.
8. Liu, J.; Xue, D., Hollow Nanostructured Anode Materials for Li-Ion Batteries. *Nanoscale research letters* 2010, *5* (10), 1525-1534.
9. Hu, L.; Wu, H.; Hong, S. S.; Cui, L.; McDonough, J. R.; Bohy, S.; Cui, Y., Si nanoparticle-decorated Si nanowire networks for Li-ion battery anodes. *Chemical communications* 2011, *47* (1), 367-9.
10. (a) Xu, X.; Cao, R.; Jeong, S.; Cho, J., Spindle-like Mesoporous α -Fe₂O₃ Anode Material Prepared from MOF Template for High-Rate Lithium Batteries. *Nano letters* 2012, *12*, 4988-4991; (b) Sun, Y.; Hu, X.; Luo, W.; Huang, Y., Self-assembled hierarchical MoO₂/graphene nanoarchitectures and their application as a

high-performance anode material for lithium-ion batteries. *ACS nano* 2011, 5 (9), 7100-7; (c) A. Magasinski; P. Dixon; B. Hertzberg; A. Kvit; Ayala, J.; Yushin, G., High-performance lithium-ion anodes using a hierarchical bottom-up approach. *Nat. Mater.* 2010, 9, 353-358; (d) Shuangling Jin; Honggui Deng; Donghui Long; Xiaojun Liu; Liang Zhan; Xiaoyi Liang; Wenming Qiao; Ling, L., Facile synthesis of hierarchically structured Fe₃O₄/carbon micro-flowers and their application to lithium-ion battery anodes. *Journal of Power Sources* 2011, 196, 3887-3893; (e) Yang, H.; Wu, X.-L.; Cao, M.-H.; Guo, Y.-G., Solvothermal Synthesis of LiFePO₄ Hierarchically Dumbbell-Like Microstructures by Nanoplate Self-Assembly and Their Application as a Cathode Material in Lithium-Ion Batteries. *J. Phys. Chem. C* 2009, 113 (8), 3345-3351; (f) Demir-Cakan, R.; Hu, Y.-S.; Antonietti, M.; Maier, J.; Titirici, M.-M., Facile One-Pot Synthesis of Mesoporous SnO₂ Microspheres via Nanoparticles Assembly and Lithium Storage Properties. *Chem. Mater.* 2008, 20 (4), 1227-1229; (g) Lin, Y.-S.; Tsai, M.-C.; Duh, J.-G., Self-assembled synthesis of nanoflower-like Li₄Ti₅O₁₂ for ultrahigh rate lithium-ion batteries. *Journal of Power Sources* 2012, 214, 314-318.

11. Lee, J. E.; Yu, S.-H.; Lee, D. J.; Lee, D.-C.; Han, S. I.; Sung, Y.-E.; Hyeon, T., Facile and economical synthesis of hierarchical carbon-coated magnetite nanocomposite particles and their applications in lithium ion battery anodes. *Energy Environ. Sci.* 2012, 5, 9528-9533.

12. (a) Hoffert, M. I.; Caldeira, K.; Benford, G.; Criswell, D. R.; Green, C.; Herzog, H.; Jain, A. K.; Kheshgi, H. S.; Lackner, K. S.; Lewis, J. S.; Lightfoot, H. D.; Manheimer, W.; Mankins, J. C.; Mauel, M. E.; Perkins, L. J.; Schlesinger, M. E.; Volk, T.; Wigley, T. M., Advanced technology paths to global climate stability: energy for a greenhouse planet. *Science* 2002, 298 (5595), 981-7; (b) Guo, K. W., Green nanotechnology of trends in future energy. *Recent patents on nanotechnology* 2011, 5 (2), 76-88; (c) Midillia, A.; Dincer, I.; Aya, M., Green energy strategies for sustainable development. *Energy policy* 2006, 34, 3623-3633; (d) Palacin, M. R., Recent advances in rechargeable battery materials: a chemist's perspective. *Chemical Society reviews* 2009, 38 (9), 2565-75; (e) John B. Goodenough, Y. K., Challenges for Rechargeable Li Batteries. *Chem. Mater* 2010, 22.

13. Cho, J.; Kim, Y. J.; Kim, T. J.; Park, B., Zero-Strain Intercalation Cathode for Rechargeable Li-Ion Cell. *Angewandte Chemie* 2001, 40 (18), 3367-3369.

14. Recham, N.; Oró-Solé, J.; Djellab, K.; Palacín, M. R.; Masquelier, C.; Tarascon, J.-M., Hydrothermal synthesis, silver decoration and electrochemistry of LiMPO₄ (M = Fe, Mn, and Co) single crystals. *Solid State Ionics* 2012, 220 (20), 47-52.

15. Choi, N. S.; Chen, Z.; Freunberger, S. A.; Ji, X.; Sun, Y. K.; Amine, K.; Yushin, G.; Nazar, L. F.; Cho, J.; Bruce, P. G., Challenges facing lithium batteries and electrical double-layer capacitors. *Angewandte Chemie* 2012, 51 (40), 9994-10024.

16. Zhang, W.-J., A review of the electrochemical performance of alloy anodes for lithium-ion batteries. *Journal of Power Sources* 2011, 196, 13-24.

17. Hassoun, J.; Derrien, G.; Panero, S.; Scrosati, B., A Nanostructured Sn-C Composite Lithium Battery Electrode with Unique Stability and High Electrochemical Performance. *Adv. Mater.* 2008, 20, 3169-3175.

18. Kim, H.; Seo, M.; Park, M. H.; Cho, J., A critical size of silicon nano-anodes for lithium rechargeable batteries. *Angewandte Chemie* 2010, 49 (12), 2146-9.

19. (a) Cabana, J.; Monconduit, L.; Larcher, D.; Palacín, M. R., Beyond Intercalation-Based Li-Ion Batteries: The State of the Art and Challenges of Electrode Materials Reacting Through Conversion Reactions.

Adv. Energy Mater. 2010, 22, E170-E192; (b) Malini, R.; Uma, U.; Sheela, T.; Ganesan, M.; Renganathan, N. G., Conversion reactions: a new pathway to realise energy in lithium-ion battery—review. *Ionics* 2009, 15, 301-307.

20. Park, C. M.; Kim, J. H.; Kim, H.; Sohn, H. J., Li-alloy based anode materials for Li secondary batteries. *Chemical Society reviews* 2010, 39 (8), 3115-41.

Chapter 2

A Facile Method to Prepare for the Ni₂P Nanostructures with Controlled Crystallinity and Morphology as Anode Materials of Lithium Ion Batteries

2.1 Introduction

A new reactivity concept based on the reversible electrochemical reaction of lithium is attracting attention in the field of LIBs due to improve the lithium ion batteries performance¹. It is called a conversion reaction. It can be expressed transition metal-anion complex. Transition metal-anion (anion = O, F, N, S, P) complex are consumed by Li ions and converted to an embedded nanometer scale metal in a lithium-anion matrix (figure 2.1)¹⁻². Conversion reaction materials have a higher theoretical capacity than insertion reaction materials due to transfer of more than one electron per 3D metal in a redox cycle (figure 2.2), and good electrical conductivity from the lithium-anion matrix and short diffusion distance from the embedded metal nanoparticle are also big advantage^{1,3}. However, conversion reaction materials have many drawbacks in terms of their use as negative electrode of LIBs. In particular, large polarization, irreversible capacity loss on first cycling, low coulombic efficiency, extreme voltage hysteresis, volume expansion during the redox cycle, and poor kinetics have not yet been resolved¹⁻².

There are a few successful strategies to overcome these problems. First of all, new nanostructured electrode design can accommodate the large volume change and improve their kinetics.^{2,4} Second, moving from bulk to thin-film material can also improve their poor kinetics problems. Third, the use of conducting coating on the particles surfaces can reduce the undesirable reactions at the interface between active materials and electrolyte and volume expansion during redox cycle.⁵ Furthermore, some researchers were reported that crystalline electrodes are replaced to amorphous materials to achieve faster conversion reaction rates.⁶ Joachim Maier et al. reported enhanced potential of an amorphous RuO₂ electrode.^{6b} And Keith J. Stevenson et al. reported a method to produce amorphous FeP₂ in high yield and with remarkable performance.^{6c} Michael R. Zachariah et al. reported that interspersed amorphous MnO_x-carbon nanocomposite provide superior electrochemical performance.^{6a}

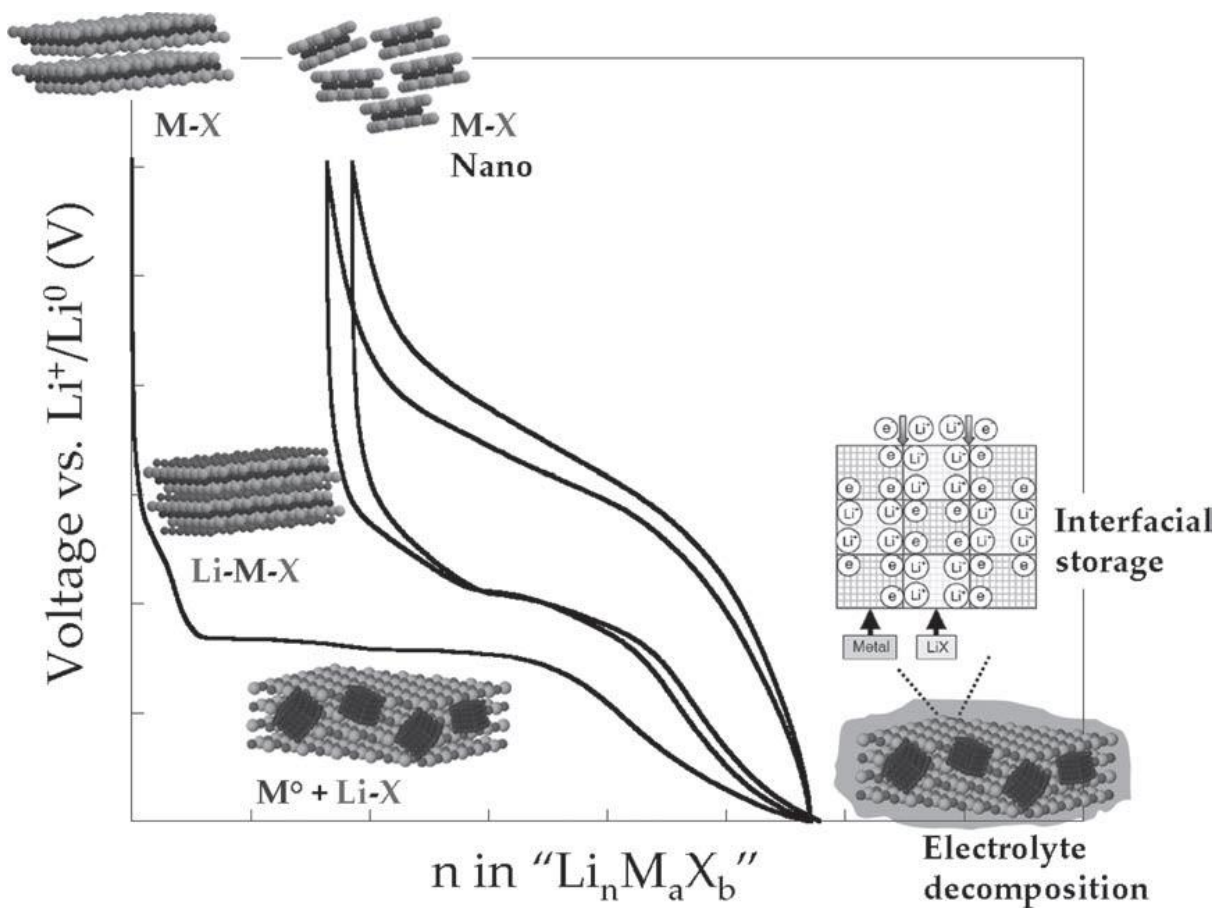


Figure 2.1 Typical voltage vs. composition profile of the conversion reaction materials.^{1b}

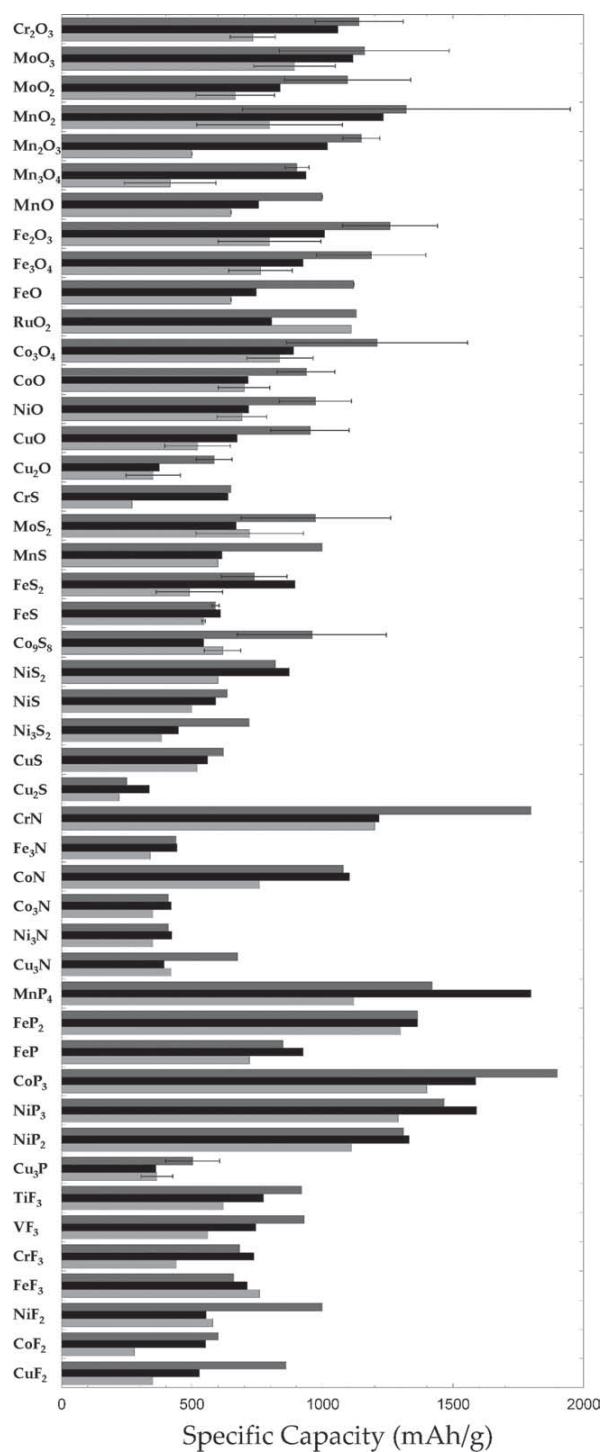


Figure 2.2 Theoretical (black bars), first discharge (dark grey), and charge (light grey) specific gravimetric capacities of different compounds that react with lithium through a conversion reaction. The experimental capacities are taken from a series of reports for each compound. The “error” bars are provided as an indication of the dispersion of values observed in the bibliography and, thus, have no statistical meaning. Data for compounds with no bar have been taken from a single literature source.^{1b}

However, there have been no reports on the difference between amorphous and crystalline electrodes in exclusion of other factors such as size differential, use of a conducting agent, different morphology, and so on. Therefore, I had the big curiosity for the effect of amorphous morphology on the conversion reaction system under identical conditions.

I am trying to introduce a facile method to prepare for the amorphous and crystalline dinickel phosphide nanoparticle clusters. Furthermore, electrochemical difference of conversion reaction between crystalline and amorphous materials with Li^+ by using nickel phosphides was analyzed.

2.2 Experimental

2.2.1. Materials

Nickel(II) acetylacetonate anhydrous ($\text{Ni}(\text{acac})_2$) 95% was purchased from Strem Chemical INC. Trioctylphosphine (TOP), technical grade 90% and Trioctylphosphine oxide (TOPO), technical grade, 90% were purchased from Sigma Aldrich Co. LLC. Chloroform and ethanol were purchased from SK Chemical. All chemicals were used without further purification.

2.2.2 Synthetic method

All of synthesis was performed by hot injection method under argon atmosphere using standard Schlenk line techniques. The Ni_2P materials were synthesized by a hot injection method in an argon atmosphere using standard Schlenk line techniques. The Ni_2P nanoparticles were prepared by the following procedure. A Ni-TOP solution was prepared by reacting 1 mmol $\text{Ni}(\text{acac})_2$ and 10 ml TOP at 60 °C until the solution became sky blue. A TOPO solution was also prepared with vigorous stirring at 330 °C. The Ni-TOP solution was added to 5 g of TOPO solution at once, and then the complex solution was maintained for 30 min. The reaction was stopped by cooling to room temperature. The nanoparticles were isolated by the addition of 30 mL of ethanol and 5 mL of chloroform followed by centrifugation. Amorphous or self-assembled Ni_2P was generated by adjusting the quantity of nickel acetylacetonate (3.57 mmol or 7.14 mmol).

2.3 Result and Discussion

The amorphous and crystalline Ni₂P nanoparticle clusters are made by hot injection method. Figure 2.3 illustrates the synthetic procedure. In the brief procedure, Ni-TOP solution and TOPO solvent were separately prepared with separately prepared vigorous stirring in three neck flask. Then, Ni-TOP solution was injected into TOPO solution at high temperature. As a result, the amorphous Ni₂P nanoparticle clusters and crystalline Ni₂P nanoparticle clusters that identical morphology and size were prepared depending on the quantity of nickel acetylacetonate. The high temperature of the bottom solution leads to instantaneous formation of nuclei, followed by slow growth.⁷ As a result, Ni₂P nanoparticles are formed. The synthetic mechanism of nickel phosphides was very well known.⁸ Our group previously reported that TOP is a good phosphorus source precursor to synthesize transition metal phosphides.^{8a,9} Because C-P bonds in TOP catalytically are cleaved when combined with some metals, P atoms can diffuse into the metal,¹⁰ thereby generating metal phosphides.

The amorphous, crystalline and self-assembled Ni₂P nanoparticles clusters are generated by adjusting the quantity of nickel acetylacetonate which followed to limit aging temperature. All synthesis is under TOP rich condition in comparison with other experiments^{8c,11} because a rich TOP act not only P source but also surfactant.

XRD patterns for the nickel phosphides reveal that dinickel phosphides were well made by hot injection method. These data were collected on a D/MAZX 2500V/PC (Rigaku) using Cu-K α radiation ($\lambda = 1.5405 \text{ \AA}$) operated for $2\theta = 10 - 80^\circ$ and with a scan rate = $2^\circ/\text{min}$. Hexagonal nickel phosphide (Ni₂P) was a perfect match with crystalline and self-assembled Ni₂P nanoparticle clusters (figure 2.4b, 2.4c). The information of broadening in the peaks of both particles implies the formation of nanometer scale particles. Furthermore, the diffraction peak of self-assembled Ni₂P nanoparticle clusters were stronger and sharper than those of crystalline Ni₂P nanoparticle clusters, indication that self-assembled Ni₂P nanoparticle clusters have higher crystallinity than that of crystalline Ni₂P nanoparticle clusters. Unlike other samples, figure 2.4a have only broad peak at about 45° , indicating amorphous material. Additional analysis of TEM (JEOL JEM-2100, operated at 200 kV), cold-FE SEM (Hitachi s-4800) and EDS were performed to verify that sample (a) is Ni₂P.

Figures 2.5a and 2.5c show TEM images of crystalline and amorphous Ni₂P nanoparticle clusters. Figures 2.5b and 2.5d clearly demonstrate that two types of nanoparticles have similar spherical morphology and size. Each particle is on average 5 nm in diameter, and these small particles join together to form clusters. In addition, EDS measurements confirm that amorphous nanoparticle clusters are dinickel phosphides (Figure 2.5e). The ratio of components between nickel and phosphorus is almost 2:1. Cu and C come from the carbon-coated Cu substrate.

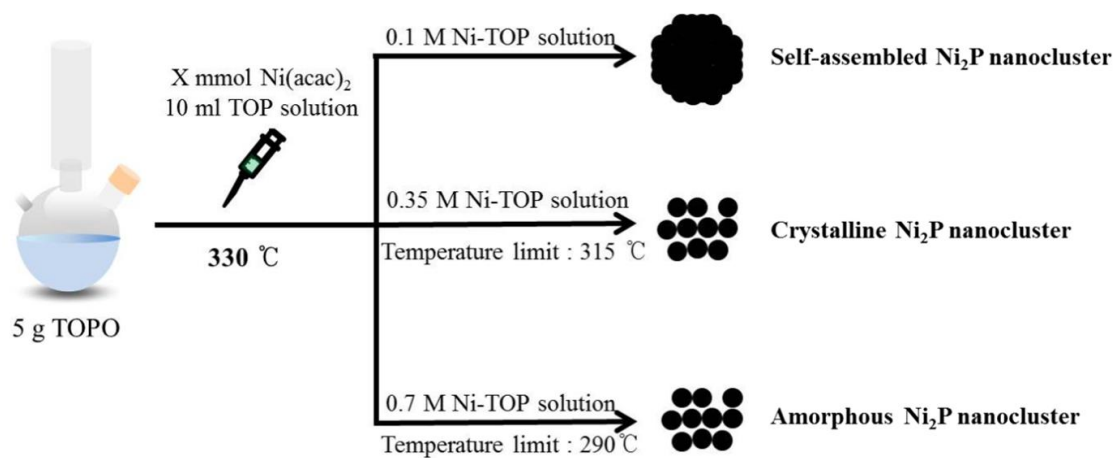


Figure 2.3 Schematic illustration of the formation of nickel phosphides

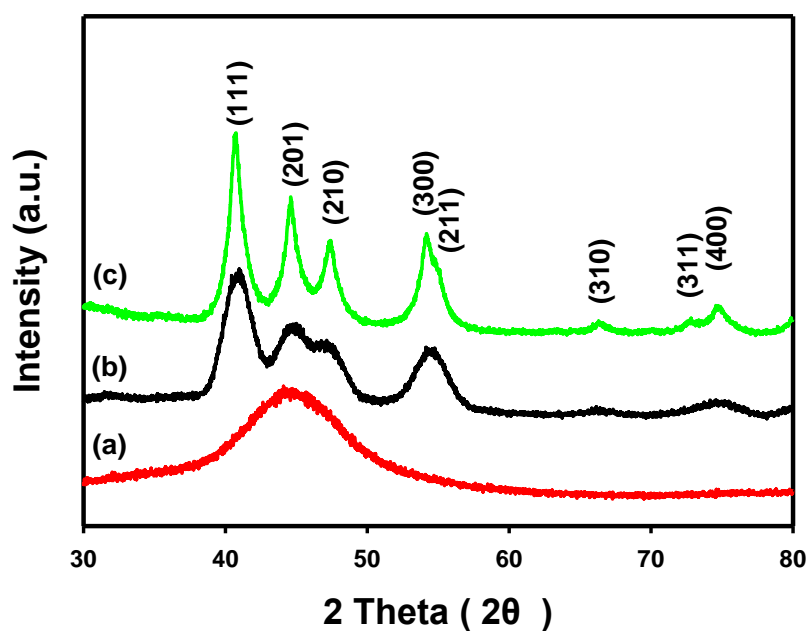


Figure 2.4 High power-XRD data of (a) amorphous Ni₂P nanoparticle clusters (b) crystalline Ni₂P nanoparticle clusters (c) self-assembled Ni₂P nanoparticle clusters.

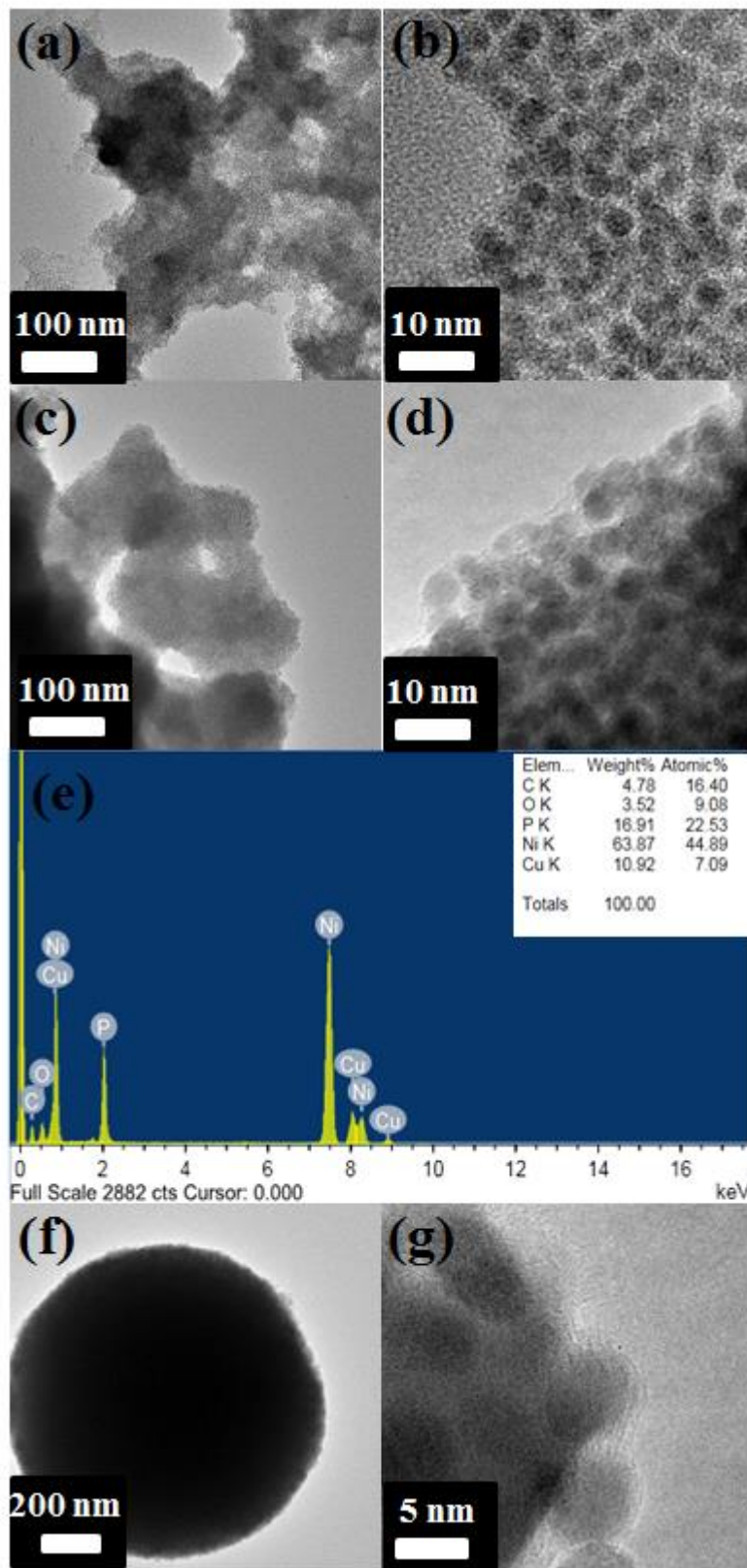


Figure 2.5 Normal TEM image of (a), (b) crystalline Ni₂P nanoparticle clusters; (c), (d) amorphous Ni₂P nanoparticle clusters; (f), (g) self-assembled Ni₂P nanoparticle clusters; EDS data of (e) amorphous Ni₂P nanoparticle clusters

The reason of different crystallinity and morphology between three samples are contributed to reaction temperature limitation by nickel precursor concentration. When the volume of injection solution (Ni-TOP solution) is based on 10 ml, introduction of 0.357 M Ni-TOP solution into bottom solution limits the reaction temperature (~ 315 °C) by the high quantity of nickel precursor, and crystalline Ni_2P nanoparticle clusters are then generated. When temperature limitation doesn't happen, crystalline Ni_2P nanoparticles converted to self-assembled Ni_2P nanoparticles clusters. A lower concentration (0.1 M) does not impose a temperature limitation, and hence high reaction temperature (330 °C) leads to the formation of s- Ni_2P nanoparticle clusters (figure 2.5e). When the concentration of Ni-TOP solution is higher than 0.714 M, amorphous Ni_2P nanoparticles clusters are formed due to the low reaction temperature (~ 290 °C) by the nickel precursor. Low aging temperature (below 300 °C) leads to amorphous Ni_2P nanoparticles^{11b} and a large amount of undecomposed TOP cause the nanoparticles to cluster.

I also did experiment about low volume/high concentration experiments for unveil reason of self-assembly of Ni_2P nanoparticles. The quantity of nickel precursor fixed at 0.5 mmol by reducing the amount of TOP to 5, 2, 1 ml, the overall concentration of injection solution increase to 0.1 M, 0.25 M and 0.5 M for maintain the reaction temperature (330 °C). The morphology of all samples show self-assembled structure regardless of concentration of injection solution (figure 2.6). This means that the reaction temperature is predominant on shape controlling of crystalline Ni_2P than injection solution concentration. However, self-assembled spherical morphology is collapsed by decreasing the amount of TOP.

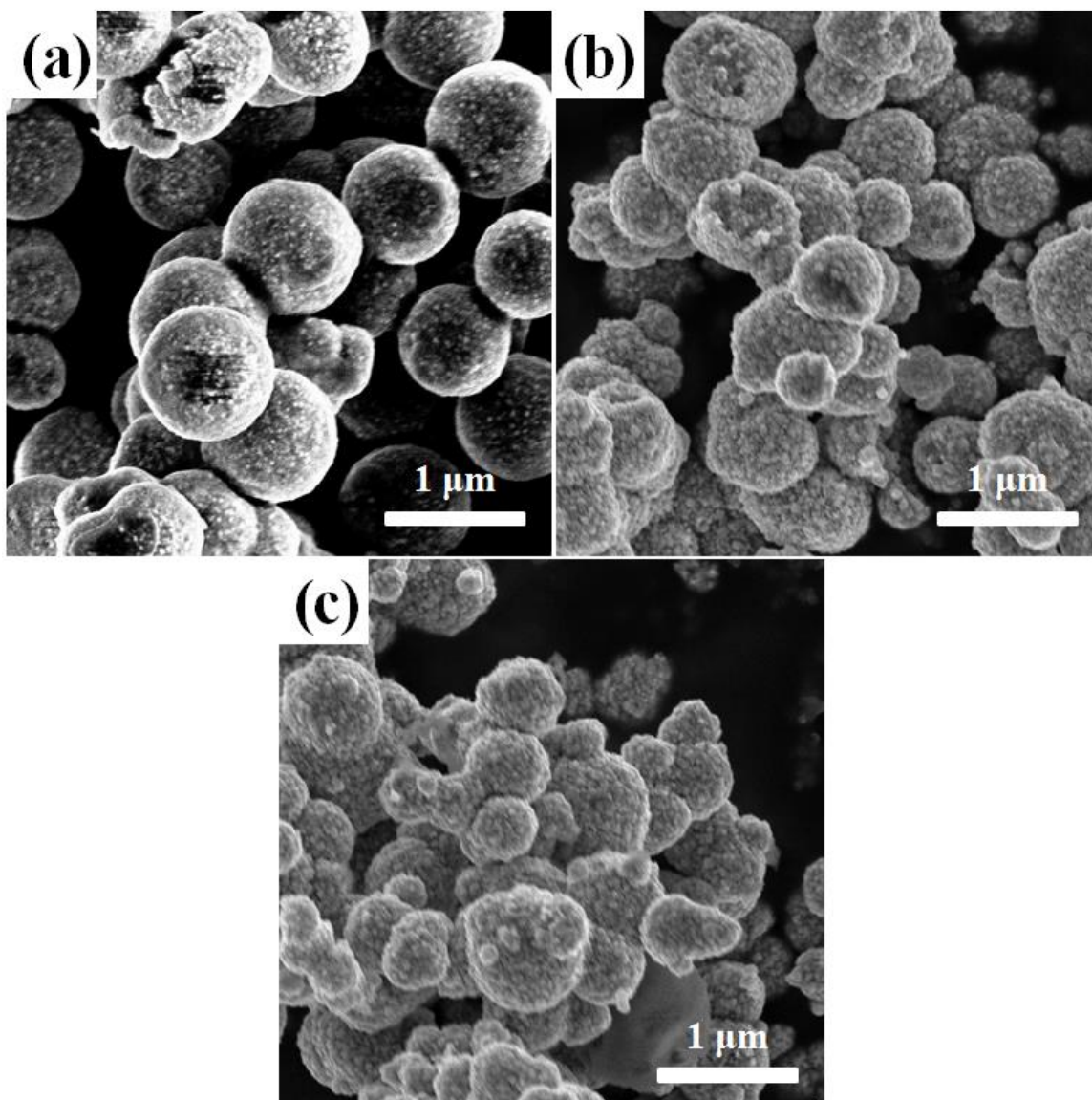


Figure 2.6 SEM image of self-assembled Ni_2P nanoparticle cluster by concentration of Ni-TOP solution; (a) 0.1 M (b) 0.25 M (c) 0.5 M

Electrochemical measurements were performed on a 2016 coin-type half-cell, where Li metal foil was used as the counter electrode, for unveil electrochemical difference of conversion reaction between crystalline and amorphous materials with Li^+ by using dinickel phosphides. The working electrodes were fabricated using a slurry mixture of active materials (dinickel phosphides, 75 wt. %), super P (15 wt. %), and polyvinylidene fluoride (PVDF) binder (LG Chem. 10%) in *N*-methylpyrrolidinone (NMP). The electrolyte was 1.3M LiPF_6 in a 3:7 volume mixture of ethylene carbonate (EC) and diethyl carbonate (DEC), and a separator was used microporous polyethylene film. Cells were assembled in an Argon-filled glove box with less than 1 ppm of both oxygen and moisture. Galvanostatic charge and discharge cycling was performed in a potential window from 0.02 to 3.0 V vs. Li/Li^+ by using WonATech WBCS 3000 battery measurement system.

Ni_2P is an attractive anode electrode materials of lithium ion batteries due to high energy density compared with conventional graphite ($\sim 372 \text{ mA h g}^{-1}$). The theoretical capacity of dinickel phosphide is 542 mAh g^{-1} . The higher theoretical capacity is contributed to transfer of more than one electron per 3D metal on redox cycle

Figure 2.7 shows the cycling performance of the Ni_2P electrodes at 0.5 C. The first discharge capacities of a- Ni_2P and c- Ni_2P electrodes were 942.6 mAh g^{-1} and 974.9 mAh g^{-1} and the reversible charge capacities were 573.2 mAh g^{-1} and 526.8 mAh g^{-1} , respectively. The higher capacities over the theoretical capacity (542 mAh g^{-1}) in the first cycle are related to decomposition of the electrolyte upon reduction with the formation of a polymeric film at low potentials and interfacial storage of Li^+ .¹² In the subsequent cycles, the a- Ni_2P electrode showed better coulombic efficiency (99.1%) and capacity retention than the c- Ni_2P electrode (96.8%).

Furthermore, reversible capacities of the two forms of Ni_2P after 50 cycles were 351.5 mAh g^{-1} and 262.9 mAh g^{-1} . The gap in the initial reversible capacity was continuously maintained throughout the cycling. In other words, the initial coulombic efficiency (ICE) is very important in conversion reaction electrodes. The gap in the ICE between the two nickel phosphides electrodes proves that a- Ni_2P is superior to c- Ni_2P at the first cycle. The a- Ni_2P nanoparticle cluster electrode has a higher ICE (average 63.61%) than the c- Ni_2P nanoparticle cluster electrode (average 58.20%) at 0.1 C, and the same results were obtained at 0.5 C (Figure 2.8). The irreversible capacity loss upon the first cycle is from the formation of a solid electrolyte interphase (SEI) layer, and irreversible conversion reaction.¹

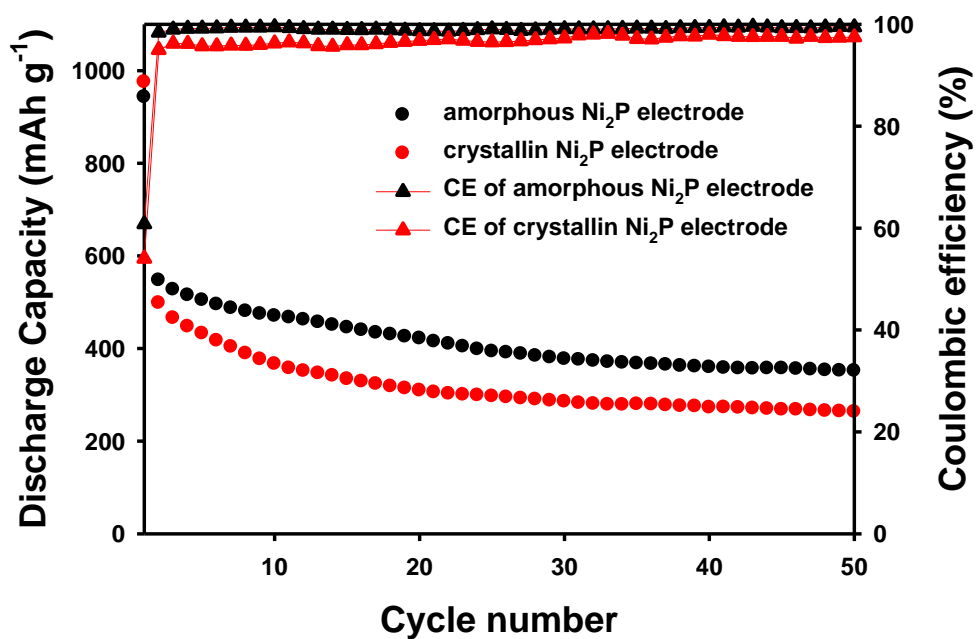


Figure 2.7 Cyclic performance of Ni₂P nanoparticle cluster electrodes at 0.5 C

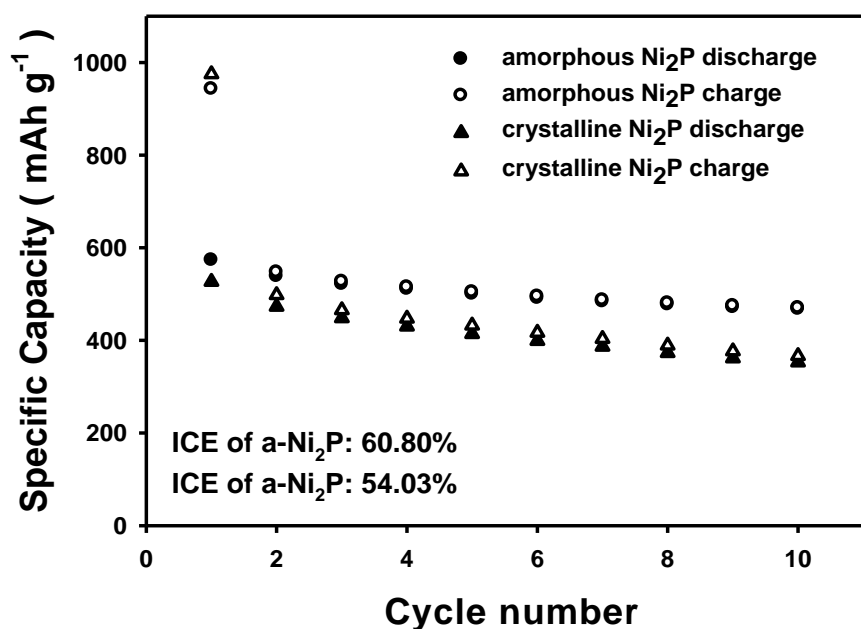


Figure 2.8 Charge and discharge capacities of Ni₂P nanoparticle cluster electrodes at 0.5 C

To shed light on this irreversible capacity gap of both electrodes upon first cycling, we analyze both electrodes by the galvanostatic intermittent titration technique (GITT). Figure 2.9 shows the GITT curves of the two electrodes. The relaxation time is 4 hr. It is well known that the upon first cycling nickel phosphides convert to Li_3P and Ni with an intermediate step of an insertion reaction.^{1b, 4b} In the initial normalized capacity region, the plateau indicates that Ni_2P forms intermediate $\text{Li}_x\text{-Ni}_2\text{P}$ by an insertion reaction due to the covalence of the nickel phosphides. Another plateau represents the conversion process where $\text{Li}_x\text{-Ni}_2\text{P}$ and lithium convert to a Li_3P matrix and nickel metal.^{1b} The polarization between CCV and QOCV after 4 hr relaxation at the first cycling is indicated in figure 2.11. In initial discharge region, polarization of amorphous Ni_2P was higher than that of crystalline Ni_2P . However, the polarization reversed during the discharge process. The polarization can represent the resistance by the equation $V = IR$ because the current is constant. Therefore, the results indicate that the resistances of both electrodes were reversed in the middle of the reaction. This reversal of resistance is due to additional resistance under amorphization of the crystalline Ni_2P electrode. Amorphous electrodes can react with lithium as solid solution behavior without a phase transition.¹³ Therefore, the amorphous Ni_2P electrode has reduced resistance because the loss of electrical contact between particles during the conversion reaction by large volume changes and structural stresses are reduced. After the region of insertion process, the polarization of both electrodes sharply decreases in the first discharge process because Ni_2P converts to a $\text{Ni/Li}_3\text{P}$ complex, which has good electronic conductivity by way of the conversion process.¹⁴

The large voltage hysteresis is one of the features of the conversion process.^{1b} It is due to increased surface area undergone by the active material in the discharge process. Another factor that contributes to large voltage hysteresis is the difference in the Gibbs free energy in the equilibrium reaction potential.¹ Comparing the electrodes, the a- Ni_2P electrode has lower voltage hysteresis than the c- Ni_2P electrode for the conversion reaction between the first lithiation and delithiation process (figure 2.12b). This is a critical factor to improve the initial coulombic efficiency of the conversion process.^{1b} Furthermore, the gap of the voltage hysteresis between the two electrodes is continuously maintained throughout cycling. The voltage hysteresis curve between the 1st charge and the 2nd discharge profile (figure 2.12a) and the gap of QOCV from the GITT curve also indicated that a- Ni_2P has lower voltage hysteresis than c- Ni_2P . This is ascribed, at least in part, to amorphization of crystalline Ni_2P , which has enhanced Gibbs free energy. The above results suggest that a- Ni_2P may achieve a faster conversion reaction and lower volume expansion than the c- Ni_2P electrode.^{6a} This is a very interesting result because large voltage hysteresis between charge and discharge is a major obstacle to commercialize conversion materials due to diminished round-trip efficiency of the electrode.^{1b}

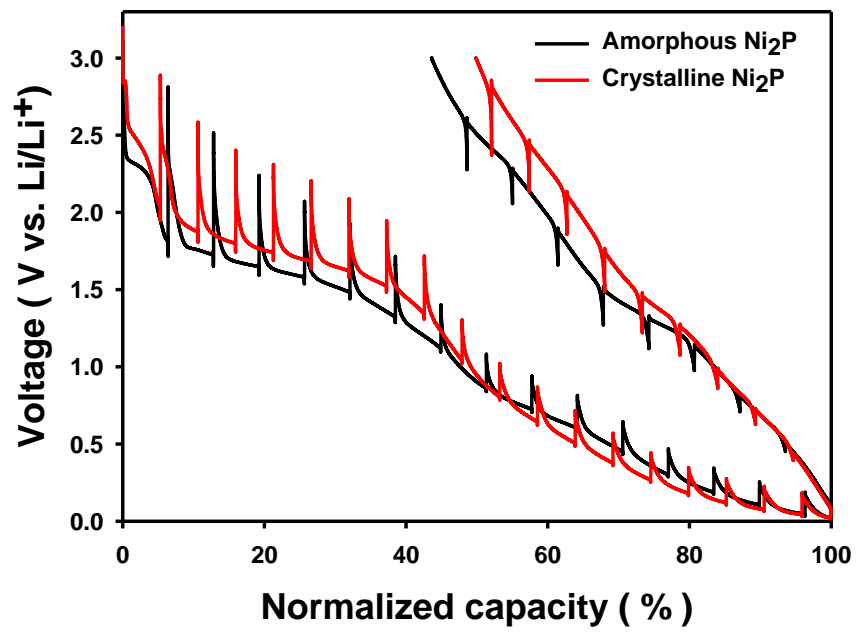


Figure 2.9 GITT curves of amorphous and crystalline Ni₂P electrodes in first cycle.

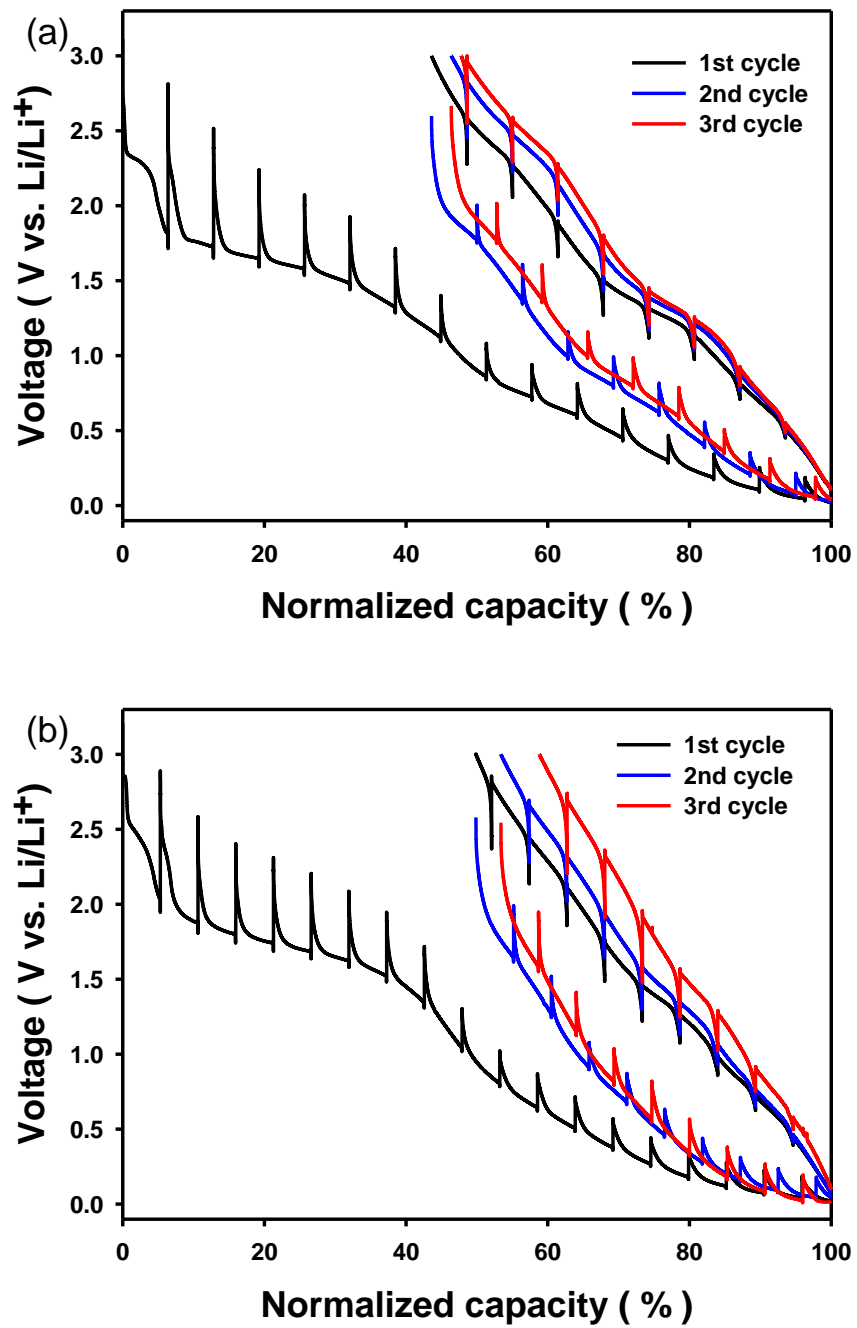


Figure 2.10 GITT curve of (a) amorphous Ni_2P electrode (b) crystalline Ni_2P electrode

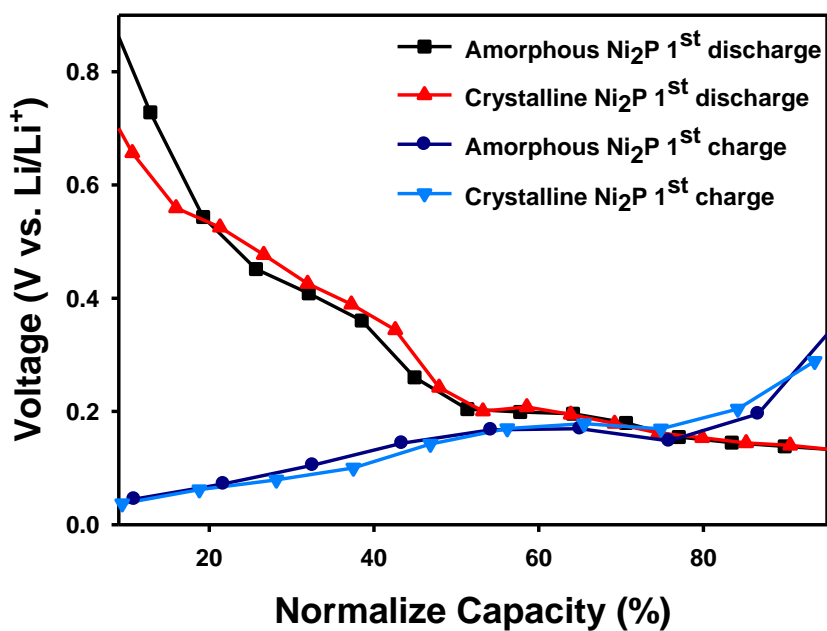


Figure 2.11 Voltage difference from GITT curve between close circuit voltage and open circuit voltage on 1st discharge and charge process

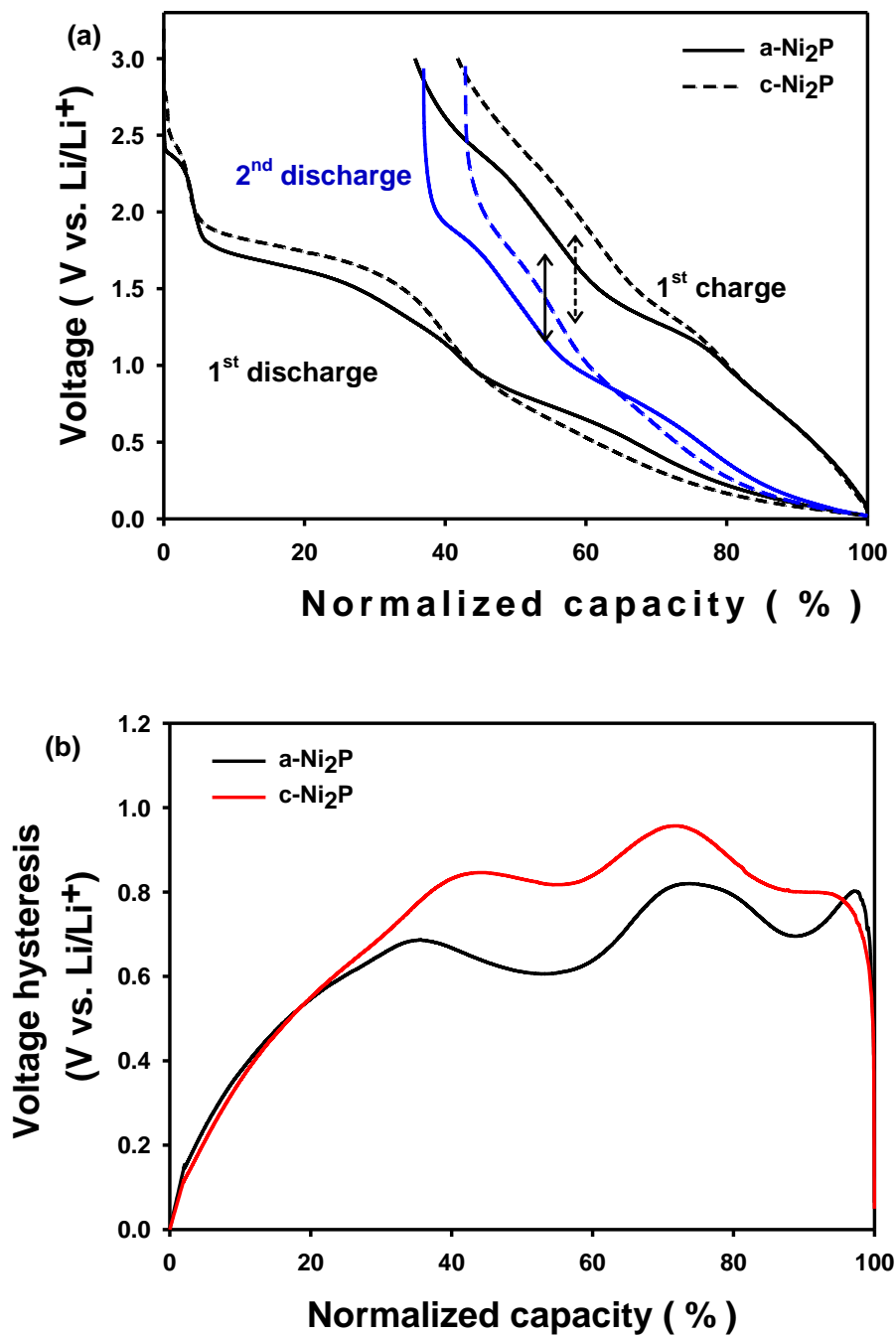


Figure 2.12 (a) 1st cycle and 2nd discharge curve of nickel phosphide electrodes. (b) Voltage hysteresis curve between 1st charge and 2nd discharge profile.

The volume expansion of electrodes during lithiation and delithiation was measured through ex situ measurement of the electrode thickness (figure 2.13). All cells were cycled for 0.1 C at 30 °C in a potential range of 0.02 to 3.0 V versus Li/Li⁺. After full lithiation until the redox potential of the working electrode reached 0.02 V vs. Li/Li⁺, the c-Ni₂P and a-Ni₂P electrodes led to considerably smaller volume expansion than the theoretical volume expansion because the nanostructure reduces the mechanical strain induced by volume change.^{2, 12, 15} In addition, the amorphous Ni₂P electrode showed considerable volume expansion of about 120%, whereas the c-Ni₂P electrode displayed a thickness change of about 164% in the fully lithiated state.

Figure 2.14 shows the electrochemical behavior of the a-Ni₂P and c-Ni₂P nanoparticle cluster electrodes characterized by cyclic voltammograms (CV) at a scanning rate of 0.2 mV s⁻¹ between 0.02 and 3 V. The small anodic peak of a-Ni₂P at 1.80 V implies that Ni₂P reacts with Li⁺ by an insertion process. The maximum reduction peak of a-Ni₂P is located at 0.66 V. The maximum peaks indicate that Li_x-Ni₂P decomposes to not only metallic Ni and a Li₃P matrix but also forms SEI.^{4b, 16} For crystalline Ni₂P, these peaks shift to 1.93 V/0.94 V. Comparing the intensity of the redox peaks of both electrodes, the peaks of the amorphous Ni₂P electrode are sharper than those of crystalline Ni₂P. In particular, the second oxidation peak of the amorphous Ni₂P electrode, which is evidently higher than the others, suggests that the amount of reversible reaction equation 1 is larger than that of the c-Ni₂P electrode.^{4b, 17}

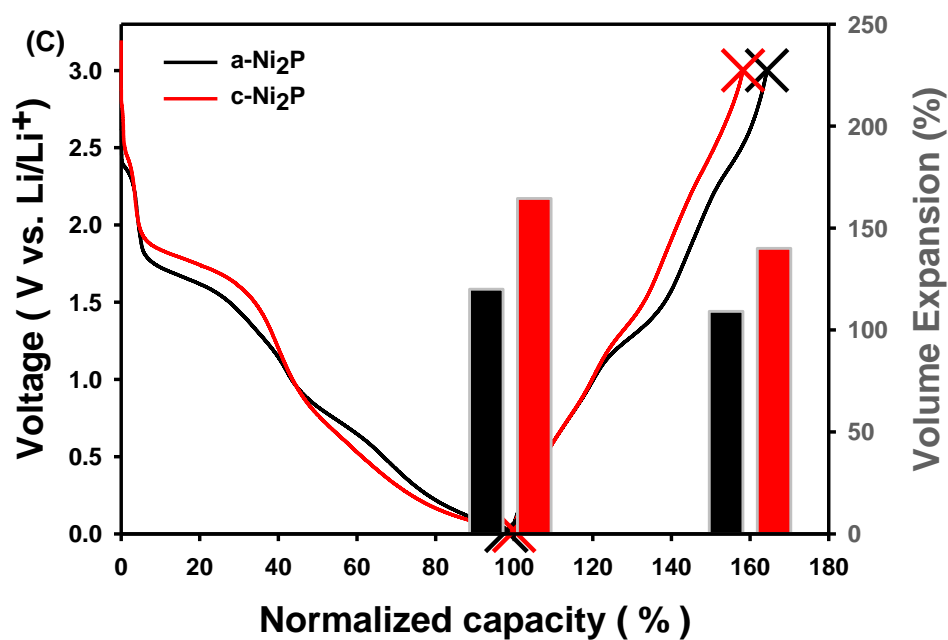
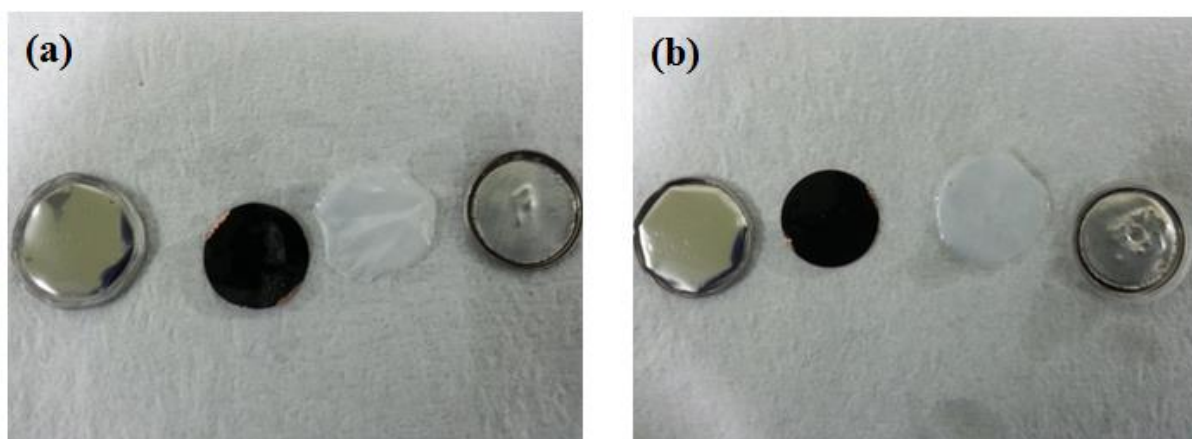


Figure 2.13 (a), (b) images of 2016 coin type half-cell after fully lithiation (c) Voltage profiles (solid line) of Ni₂P nanoparticles clusters electrodes and the corresponding electrode thickness change (bar) during lithiation and delithiation.

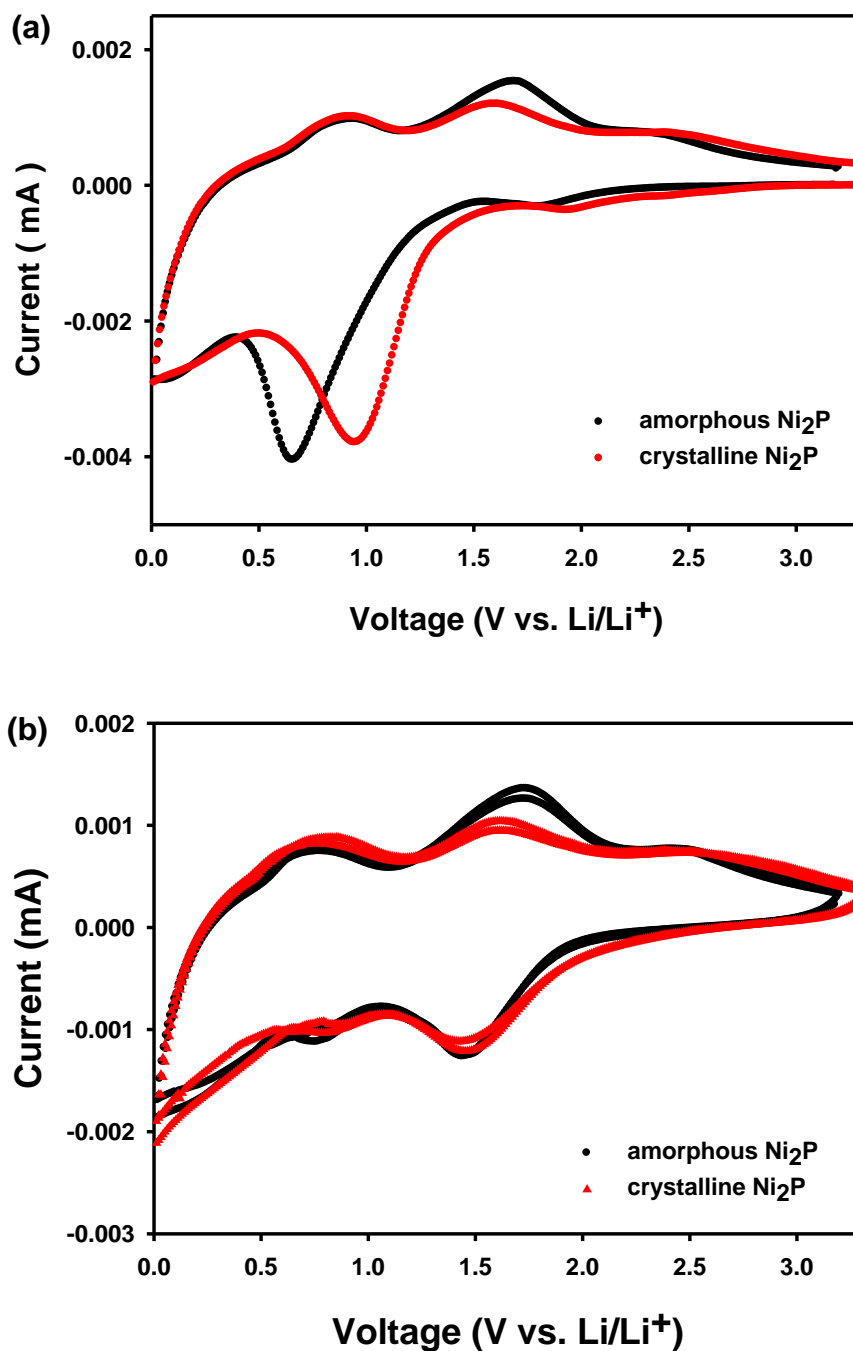


Figure 2.14 CV curves of amorphous Ni₂P and crystalline Ni₂P electrodes for (a) the first cycle and (b) the second and third cycles at a scan rate of 0.2 mV s⁻¹ from 0.02 to 3.0 V.

2.4 Conclusions

Crystalline and amorphous nickel diphosphide nanoparticles clusters that have almost same shape and size were synthesized by a simple hot injection method. This was achieved by adjusting the quantity of nickel acetylacetonate, which made it possible to limit the aging temperature. Furthermore, its electrochemical characteristics were investigated to analyze the effect of amorphous morphology on the conversion reaction in a LIB. These materials were characterized by TEM, SEM, XRD, and EDS. From the characterization, amorphous and crystalline spherical ~5 nm clusters have almost the same size and structure. In addition, self-assembled Ni₂P nanoparticle clusters could be generated at 330 °C without oleylamine. The electrochemical results showed that amorphous materials in isolation from other factors can be used to overcome the problems impeding conversion reaction materials, such as low initial coulombic efficiency, large voltage hysteresis, capacity retention, and serious volume expansion. Amorphous Ni₂P provides superior initial coulombic efficiency over the crystalline materials in the conversion reaction with Li⁺ because there is no amorphization process. In addition, amorphous nickel phosphide can reduce voltage hysteresis and volume expansion during cycling, which are very serious obstacles to the commercialization of conversion materials. In the future, it will be of significant interest to synthesize amorphous nanometer scale conversion materials such as iron oxides, and manganese oxides.

2.5 Reference

1. (a) Malini, R.; Uma, U.; Sheela, T.; Ganesan, M.; Renganathan, N. G., Conversion reactions: a new pathway to realise energy in lithium-ion battery. *Ionics* **2009**, *15*, 301-307; (b) Cabana, J.; Monconduit, L.; Larcher, D.; Palacín, M. R., Beyond Intercalation-Based Li-Ion Batteries: The State of the Art and Challenges of Electrode Materials Reacting Through Conversion Reactions. *Adv. Energy Mater.* **2010**, *22*, E170-E192.
2. Boyanov, S.; Annou, K.; Villeveille, C.; Pelosi, M.; Zitoun, D.; Monconduit, L., Nanostructured transition metal phosphide as negative electrode for lithium-ion batteries. *Ionics* **2008**, *14*, 183–190.
3. Cheng, F.; Liang, J.; Tao, Z.; Chen, J., Functional materials for rechargeable batteries. *Adv. Mater.* **2011**, *23* (15), 1695-715.
4. (a) Arico, A. S.; Bruce, P.; Scrosati, B.; Tarascon, J. M.; van Schalkwijk, W., Nanostructured materials for advanced energy conversion and storage devices. *Nat Mater* **2005**, *4* (5), 366-77; (b) Lu, Y.; Tu, J. P.; Xiong, Q.; Qiao, Y.; Wang, X.; Gu, C.; Mao, S. X., Synthesis of dinickel phosphide (Ni₂P) for fast lithium-ion transportation: a new class of nanowires with exceptionally improved electrochemical performance as a negative electrode. *RSC Adv* **2012**, *2*, 3430-3436; (c) Jang, B.; Park, M.; Chae, O. B.; Park, S.; Kim, Y.; Oh, S. M.; Piao, Y.; Hyeon, T., Direct Synthesis of Self-Assembled Ferrite/Carbon Hybrid Nanosheets for High Performance Lithium-Ion Battery Anodes. *J. Am. Chem. Soc.* **2012**, *134*, 15010-15015; (d) Xu, X.; Cao, R.; Jeong, S.; Cho, J., Spindle-like mesoporous α -Fe(2)O(3) anode material prepared from MOF template for high-rate lithium batteries. *Nano Lett* **2012**, *12* (9), 4988-91.
5. (a) Jang, B.; Park, M.; Chae, O. B.; Park, S.; Kim, Y.; Oh, S. M.; Piao, Y.; Hyeon, T., Direct Synthesis of Self-Assembled Ferrite/Carbon Hybrid Nanosheets for High Performance Lithium-Ion Battery Anodes. *Journal of the American Chemical Society* **2012**, *134*, 15010-15015; (b) Xu, X.; Cao, R.; Jeong, S.; Cho, J., Spindle-like Mesoporous α -Fe₂O₃ Anode Material Prepared from MOF Template for High-Rate Lithium Batteries. *Nano letters* **2012**, *12*, 4988-4991.
6. (a) Guo, J.; Liu, Q.; Wang, C.; Zachariah, M. R., Interdispersed Amorphous MnOx–Carbon Nanocomposites with Superior Electrochemical Performance as Lithium-Storage Material. *Adv. Funct. Mater.* **2012**, *22*, 803-811; (b) Delmer, O.; Balaya, P.; Kienle, L.; Maier, J., Enhanced Potential of Amorphous Electrode Materials: Case Study of RuO₂. *Adv. Mater.* **2008**, *20*, 501-505; (c) Hall, J. W.; Membreno, N.; Wu, J.; Celio, H.; Jones, R. A.; Stevenson, K. J., Low-Temperature Synthesis of Amorphous FeP₂ and Its Use as Anodes for Li Ion Batteries. *J. Am. Chem. Soc.* **2012**, *134*, 5532-5535; (d) Zhang, H.; Lu, Y.; Gu, C. D.; L., W. X.; Tu, J. P., Ionothermal synthesis and lithium storage performance of core/shell structured amorphous@crystalline Ni–P nanoparticles. *CrystEngComm* **2012**, *14*, 7942-7950.
7. Doneg, C. M.; Liljeroth, P.; Vanmaekelbergh, D., Physicochemical Evaluation of the Hot-Injection Method, a Synthesis Route for Monodisperse Nanocrystals. *Small* **2005**, *1* (25), 1152-1162.
8. (a) Park, J.; Koo, B.; Yoon, K. Y.; Hwang, Y.; Kang, M.; Park, J. G.; Hyeon, T., Generalized Synthesis of Metal Phosphide Nanorods via Thermal Decomposition of Continuously Delivered Metal-Phosphine Complexes Using a Syringe Pump. *J. Am. Chem. Soc.* **2005**, *127*, 8433-8440; (b) Chen, Y.; She, H.; Luo, X.; Yue, G. H.; Peng, D. L., Solution-phase synthesis of nickel phosphide single-crystalline nanowires. *J Cryst Growth* **2009**, *311*, 1229-1233; (c) Muthuswamy, E.; Savithra, G. H. L.; L., B. S., Synthetic Levers Enabling

Independent Control of Phase, Size, and Morphology in Nickel Phosphide Nanoparticles. *Acs Nano* **2011**, *5* (3), 2402-2411.

9. Park, J.; Koo, B.; Hwang, Y.; Bae, C.; An, K.; Park, J. G.; Park, H. M.; Hyeon, T., Novel Synthesis of Magnetic Fe₂P Nanorods from Thermal Decomposition of Continuously Delivered Precursors using a Syringe Pump. *Angew. Chem* **2004**, *116*, 2332-2335.

10. Chen, J. H.; Tai, M. F.; Chi, K. M., Catalytic synthesis, characterization and magnetic properties of iron phosphide nanowires. *J Mater Chem* **2004**, *14*, 296-298.

11. (a) Schaak, A. E. H. a. R. E., Trioctylphosphine: A General Phosphorus Source for the Low-Temperature Conversion of Metals into Metal Phosphides. *Chem. Mater* **2007**, *19*, 4234-4242; (b) Wang, J.; Johnston-Peck, A. C.; Tracy, J. B., Nickel Phosphide Nanoparticles with Hollow, Solid, and Amorphous Structures. *Chem. Mater* **2009**, *21*, 4462-4467.

12. Ponrouch, A.; Taberna, P. L.; Simon, P.; Palacín, M. R., On the origin of the extra capacity at low potential in materials for Li batteries reacting through conversion reaction. *Electrochim Acta* **2012**, *61*, 13-18.

13. Larcher, D.; Beattie, S.; Morcrette, M.; Edstrom, K.; Jumas, J. C.; tarascon, J. M., Recent findings and prospects in the field of pure metals as negative electrodes for Li-ion batteries. *J Mater Chem* **2007**, *17*, 3759-3772.

14. Sauvage, F.; Tarascon, J. M.; Baudrin, E., In Situ Measurements of Li Ion Battery Electrode Material Conductivity: Application to Li_xCoO₂ and Conversion Reactions. *J. Phys. Chem. C* **2007**, *111*, 9624-9630.

15. Kim, H.; Seo, M.; Park, M. H.; Cho, J., A Critical Size of Silicon Nano-Anodes for Lithium Rechargeable Batteries. *Angew. Chem. Int. Ed.* **2010**, *49*, 2146-2149.

16. Lu, Y.; Tu, J. P.; Xiang, Y. J.; Wang, X. L.; Zhang, J.; Mai, Y. J.; Mao, S. X., Improved Electrochemical Performance of Self-Assembled Hierarchical Nanostructured Nickel Phosphide as a Negative Electrode for Lithium Ion Batteries. *J. Phys. Chem. C* **2011**, *115*, 23760-23767.

17. Lu, Y.; Tu, J. P.; Xiong, Q.; Qiao, Y.; Zhang, J.; Gu, C.; Wang, X.; Mao, S. X., Carbon-Decorated Single-Crystalline Ni₂P Nanotubes Derived from Ni Nanowire Templates: A High-Performance Material for Li-Ion Batteries. *Chem. Eur. J* **2012**, *18*, 6031-6038.

Chapter 3

Graphene Oxide-Assisted Synthesis of Self-Assembled Zinc Oxide for Lithium-Ion-Battery Anode

3.1 Introduction

Nanostructured electrodes for lithium ion batteries have benefits such as new reaction mechanisms that are not possible with bulk materials, short pathways of Li^+ ion and electron transport, better buffering of volume expansion. However, the commercial application of such materials requires overcoming the challenges such as poor cycle retention due to an increase in undesirable electrode/electrolyte reactions caused by the greater surface area, low volumetric energy densities due to the inferior packing of nanoparticles, and the high cost of complicated synthesis processes.¹ There has already been a variety of approaches made to overcome some of these issues, such as forming composites with carbon or a conductive agent, or using assembled, hollow, or core-shell structures² More recently, self-assembled structures with a carbon coating have emerged as a promising candidate for the cathode and anode material of lithium-ion batteries (LIBs). Such self-assembled structures have the potential to not only reduce the transport pathways of Li^+ ions and electrons but also reduce the unwanted side reactions between the electrodes and the electrolyte.³ Moreover, their porous nature provides a volume of free space that help can accommodate the intense volume expansion of electrodes during cycling.^{3b-d} The carbon coating acts to improve the overall electrical conductivity and mechanical strength, ensures the formation of a stable solid electrolyte interface (SEI), and helps prevent self-aggregation of the nanoparticles.^{2a, 4} Although various methods have been previously developed for fabricating a self-assembled structure, these approaches tend to be based on either inert conditions or to rely on complex high-temperature and high-pressure process.^{3d, 5} Moreover, such methods often lack a convenient means of carbon coating after synthesis of the active material.^{3c} Above hash conditions or complex process results in a high cost or difficulty of commercialization.

To overcome these problems, a simple one-step method for the reduced graphene oxide-assisted synthesis of a hierarchical self-assembled zinc oxide (SAZO) is described, and the suitability of the resulting material as LIB anode is evaluated.

3.2 Experimental

3.2.1. Materials

Zinc acetate, 99.99% trace metals basis, was purchased from Sigma Aldrich Co. LLC. Graphene Oxide (GO) was prepared from graphite powder (Bay carbon Inc.) by a modified Hummers method.⁶ *N,N*-dimethylformamide, HPLC grade, was purchased from Samchum Pure Chemicals. Ethanol was purchased from SK Chemical. All chemicals were used without further purification.

3.2.2 Synthetic method

In a typical synthesis of self-assembled zinc oxide (SAZO)@rGO, Zinc acetate ((CH₃CO₂)₂Zn, 0.92 g) was added to *N,N*-dimethylformamide (DMF, 200 mL). The mixture was stirred for 20 min at the room temperature. Graphene oxide (GO, 40 mg) was also dissolved in 50 mL DMF and sonicated for 30 min. Then, graphene oxide solution was added to zinc acetate solution under vigorous stirring. The colorless solution change dark blue color. The mixture was heated to 95~125 °C under continuous stirring. After keeping 5 h at 70~125 °C, the result products were isolated by the addition of ethanol and DI water followed by centrifugation. The result powder was transferred to a quartz tube furnace and annealed at 500 °C with Argon gas for 3 hr.

In case of synthesis of doughnut-like zinc oxide (DLZO)@rGO is almost same with that of SAZO@rGO. Reactions were also carried out in which the solution ratio of GO solution was systematically varied in the range 0.25~4 of DMF : DI water ratio. Entire process was carried out as described for the SAZO@rGO.

3.3 Result and Discussion

3.3.1 The synthetic mechanism of SAZO@GO & Temperature tendency

The method used to synthesize the self-assembled zinc oxide (SAZO)@GO nanocomposite is illustrated in figure 3.1. The SAZO@GO composite is obtained by simply heating a mixture of zinc acetate and graphene oxide in DMF above 95 °C under atmospheric pressure, the GO having been prepared from natural graphite powder by a modified Hummers method.⁶ The results of TEM and SEM shown in Figure 1A, 1B and S2 confirm that the ZnO particles on the surface of GO are exhibit a hierarchical morphology with diameters ranging from 240 to 280 nm depending on the temperature of synthesis (figure 3.2a, 2b and 3.3a, 3b). Controllable synthesis of the self-assembled nanocomposite is accomplished with the assistance of GO. Spontaneous hydrolysis and condensation of the zinc acetate occurs due to the moisture in the air and DMF, resulting in the formation of ZnO nanoparticles.⁷ Consequently, Zn²⁺ ions chemisorbed on the surface of ZnO react with functional groups (COOH, OH) of the GO.⁸ Then, colloidal ZnO nanoparticles in DMF were going to assembly chemically linked ZnO with the GO which in turn act to stabilize the remaining ZnO.⁷ In the absence of GO, the ZnO does not form a self-assembled hierarchical morphology, but rather agglomerates of nanoparticles (figure 3.5). Therefore, controllable synthesis of a self-assembled nanocomposite is possible through assistance of GO.

Figure 3.4 depicts the X-ray diffraction (XRD) patterns of ZnO@GO composites with varying synthesis temperatures. This demonstrates that a hexagonal phase pure ZnO is formed when the synthesis temperature is above 95 °C, however, impurities are detected with synthesis temperatures below 85 °C. The TEM images suggest that impurities may still be present SAZO@GO composites generated at more than 85 °C, however, there is a notable change in particle size between the 130 to 190 nm of 85 °C sample and the 240 to 280 nm of those samples produced at 95 °C or above. In order to further understand the mechanism of ZnO formation, an aliquot of the reaction solution was taken at different stages of the process (Figure 3.6). TEM images of those aliquots removed while the temperature was still below 70 °C indicate that zinc oxide clusters are generated on the GO, but some impurities still exist. Pure self-assembled materials are identified, ranging in size from 110 nm to 150 nm, once the temperature reaches 95 °C. These particles go on to form the larger SAZO particles, reaching their maximum size of 280 nm after aging for an hour.

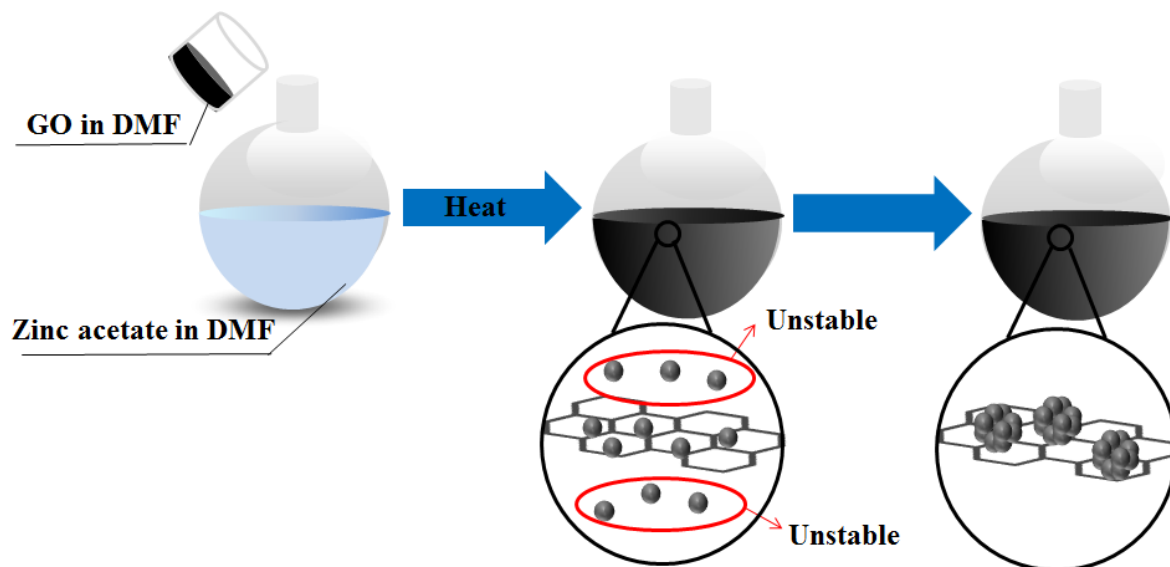


Figure 3.1. Illustration depicting the preparation of self-assembled ZnO

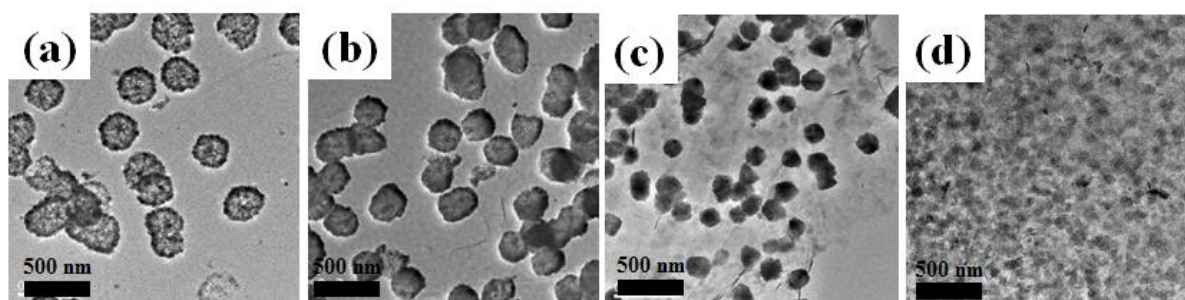


Figure 3.2 TEM images of ZnO/GO synthesized at temperatures of (A) 125 °C (B) 95 °C (C) 85 °C (D) 45 °C

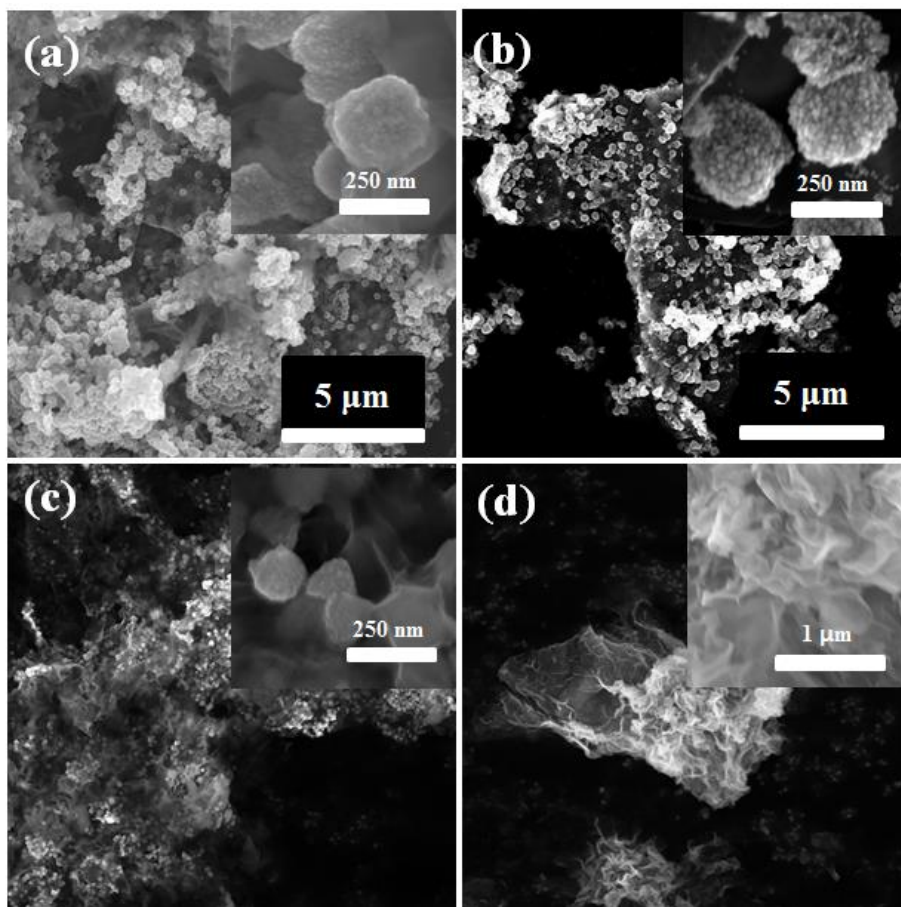


Figure 3.3 SEM images of ZnO/GO with varying temperature (A) 125 °C (B) 95 °C (C) 85 °C (D) 45 °C

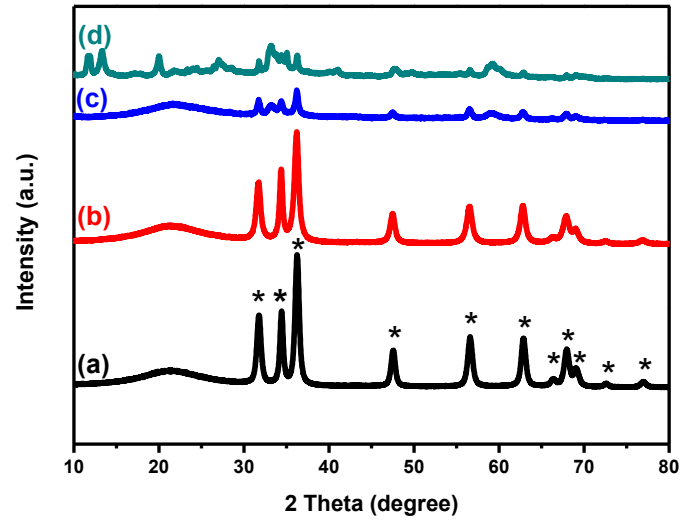


Figure 3.4 XRD patterns of ZnO/rGO with various temperatures of synthesis A) 125 °C (B) 95 °C (C) 85 °C (D) 45 °C *= Zincite

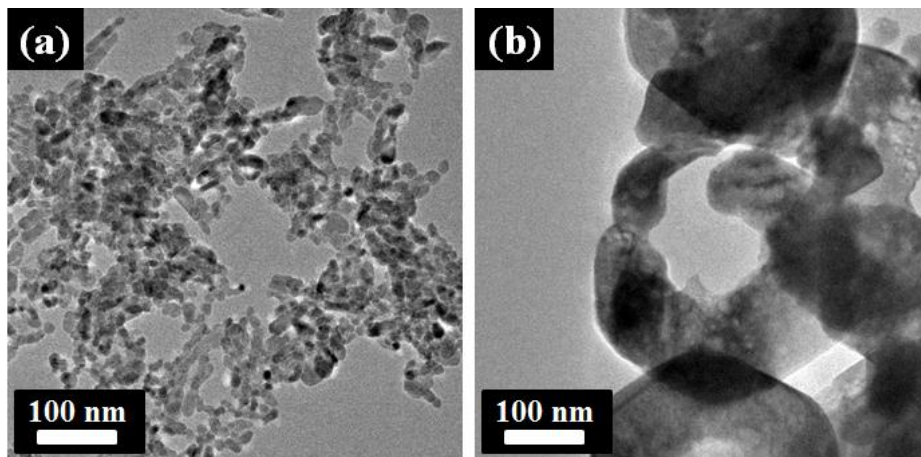


Figure 3.5 TEM images of (a) ZnO nanoparticle clusters (b) doughnut-like ZnO

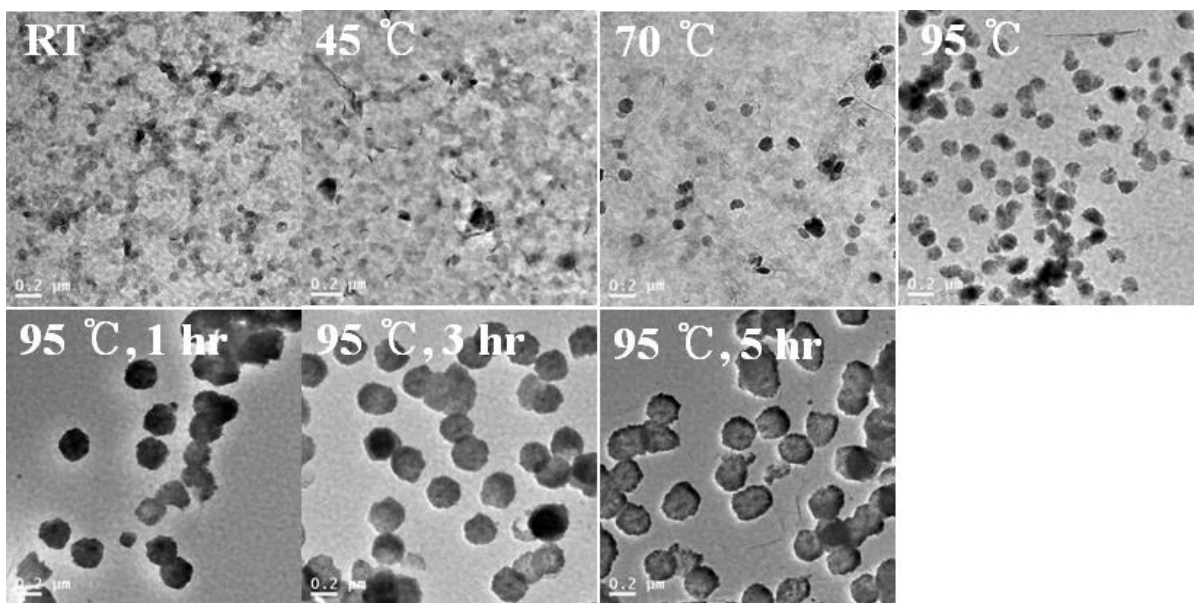


Figure 3.6 Time series of TEM image of ZnO/rGO

3.3.2 Moisture effect

Moisture is also a very significant factor deciding the final morphology of the ZnO, as it influences both hydrolysis and condensation. Synthesis was therefore conducted under inert conditions without moisture. This synthesis is performed under argon atmosphere using standard Schlenk line techniques. I also use refined DMF as a solvent after moisture was eliminated by using molecular sieve.

There is no any change in the mixture of three neck flask during a reaction when the reaction is carried out without moisture (figure 3.7). This implies that zinc oxide was not generated in non-moisture condition because hydrolysis and condensation reaction doesn't happen. After termination of reaction, the result solution was isolated by the addition of ethanol and DI water followed by centrifugation but precipitants are not generated. TEM images show that there is no zinc oxide in the solution.

In contrast, the introduction of additional DI water caused a more intense and exothermic hydrolysis and condensation reaction. If the moisture in the air and DMF at room temperature is assumed to be a negligible quantity, then 10 mL of DI water is sufficient to form a self-assembled hierarchical zinc oxide. However, a quantity of DI water greater than 25 ml results in an irregular ZnO morphology with diameters from 100 to 300 nm. Furthermore, increasing the DI water to 50 ml resulted in a doughnut-like morphology as the zinc oxide was increasingly etched from the inside with reaction time. XRD analysis of all samples, however, indicated that only a hexagonal phase ZnO was present (figure 3.10).

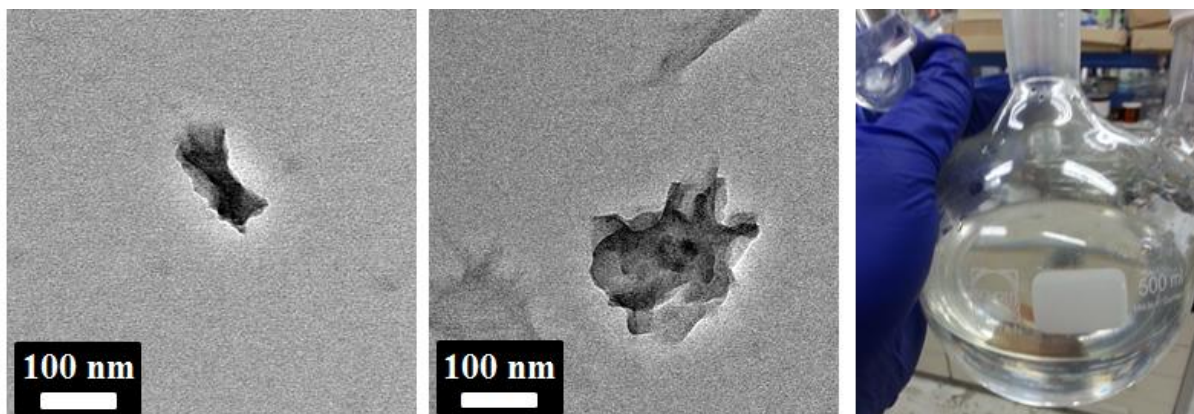


Figure 3.7 TEM images and picture of result product after ZnO synthesis at the inert condition

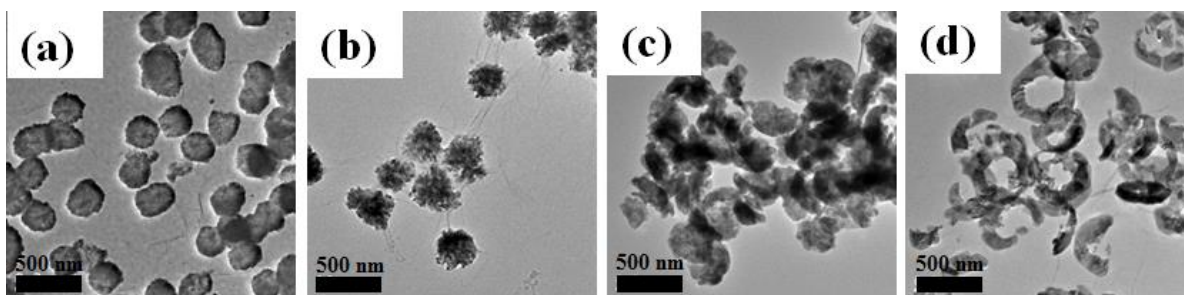


Figure 3.8 TEM images of ZnO/GO at 85 °C with various cosolvent ratios of DMF/DI water = (A) 250 : 0, (B) 240 : 10, (C) 225 : 25, and (D) 200:50.

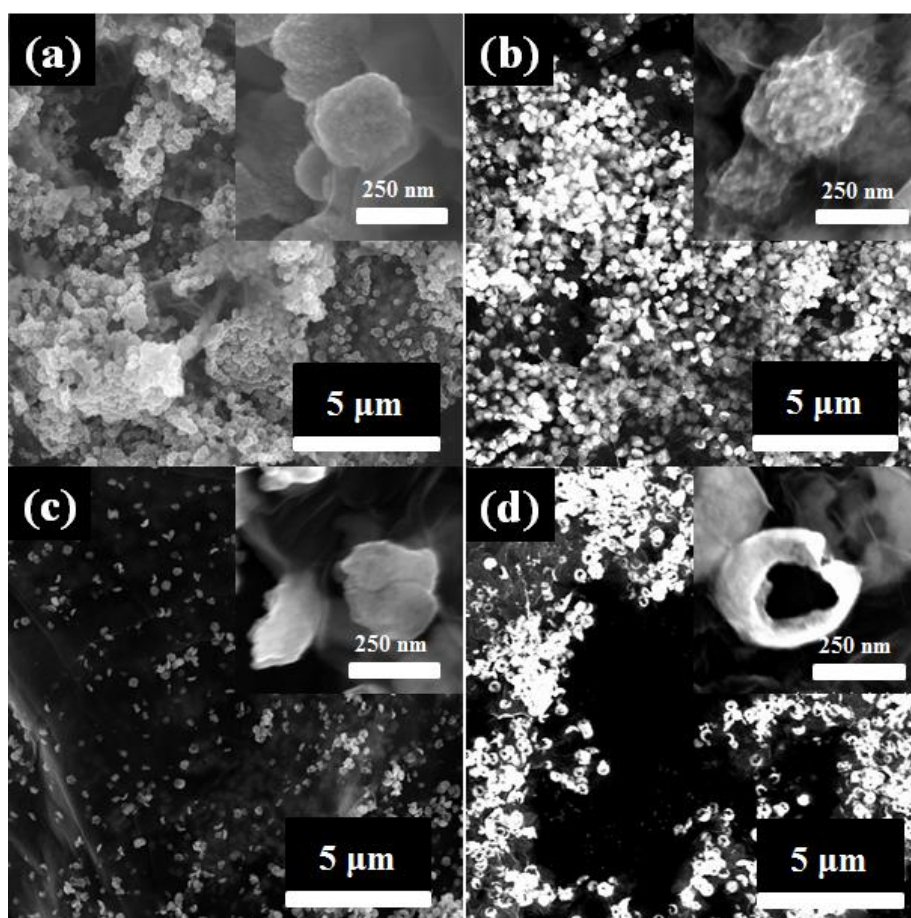


Figure 3.9 SEM images of ZnO/rGO with varying cosolvent ratios DMF : DI water = (A) 250 : 0 (B) 240 : 10 (C) 225 : 25 (D) 200 : 50

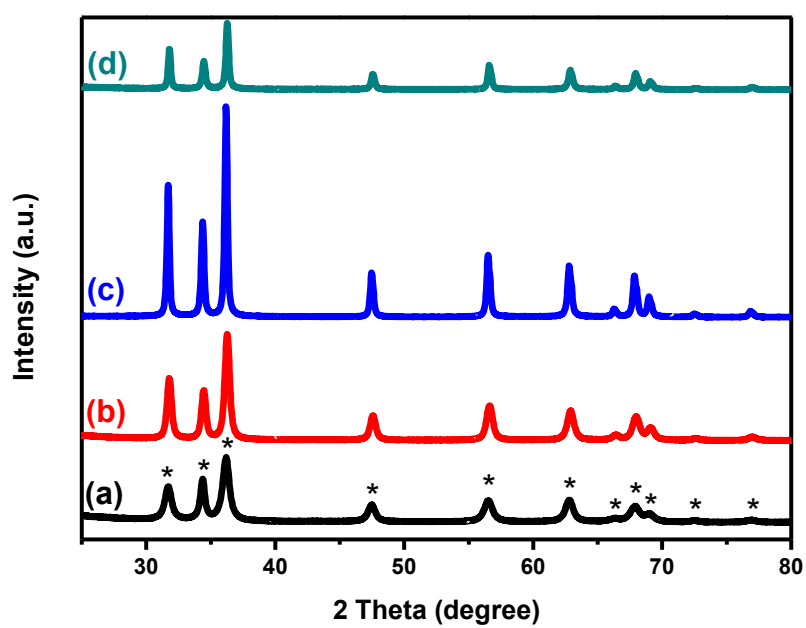


Figure 3.10 XRD patterns of ZnO/rGO with varying cosolvent ratios DMF : DI water = (A) 250 : 0 (B) 240: 10 (C) 225:25 (D) 200 : 50

3.3.3 Controlling of SAZO@rGO ratio

TGA of SAZO@GO (Figure 3.11a) conducted at temperatures up to 700 °C in Air reveals that the weight fraction of ZnO in the composite is dependent on the synthesis temperature. The small mass loss below 130 °C can be explained by the thermal removal of absorbed water, while the large mass loss of GO above 200 °C is the result of thermal decomposition. The TGA analysis confirms that the GO is entirely eliminated below 500 °C (figure 3.12). Furthermore, SEM imaging confirmed that the GO is eliminated without damage to the hierarchical morphology (figure 3.13), while XRD analysis of SAZO after calcination in air revealed that the zinc oxide is unaltered. Consequently, a high reaction temperature of 125 °C results in a ZnO weight fraction of 80.2 % in the composite, which is higher than was obtained using a lower temperature (95 °C).

3.3.4 Improving of conductivity

Though the graphene oxide is primarily considered as a host for self-assembly, when reduced it also proves to be an effective additive for increasing electrical conductivity. Hybrid nanostructures incorporating rGO sheets have been previously reported to hamper the agglomeration of nanoparticles on during cycling and improve the overall electrical conductivity.^{2b, 9} As a result, such hybrid nanostructures typically exhibit a high specific capacity and long cycle stability.⁹⁻¹⁰ The reduction of GO was achieved by transferring the samples to a quartz tube furnace and annealing them for 3 hours at 500 °C under Argon atmosphere. The XRD patterns of the resulting SAZO@rGO shown Figure 3.11b demonstrate that a hexagonal ZnO structure was retained after calcination.

To prove the reduction of GO, Raman spectra of GO and SAZO@GO before and after calcination were obtained, as shown in Figure 3C. In all samples, the two major peaks of the D and G band can observed. The D and G bands of GO are located at around 1588 and 1355 cm^{-1} , however, the G band is red shifted to 1585 cm^{-1} in SAZO@GO and to 1583 cm^{-1} in SAZO@rGO. This suggests that the synthesis process itself contributes to a shift in the G band and that additional heat treatment merely creates a further shift in the G band. The gradual increase in the I_D/I_G band intensity ratio from GO to SAZO@rGO suggests a high degree of GO reduction by heat treatment.

We also tried to measure the electronic conductivities to convince reduction of GO. Analysis of electrical conductivity using the van der Pauw method was also used to confirm the reduction of GO, the resulting data shown in Figure 3.11d.¹¹ The SAZO@GO powders have an electrical conductivity of $1.15 \times 10^{-2} \text{ S cm}^{-1}$, which is dramatically increased to $1.32 \times 10^{-1} \text{ S cm}^{-1}$ after heat treatment. This provides fairly conclusive evidence that GO is reduced to rGO and means that rGO can be used to improve the poor electrical conductivity of ZnO.

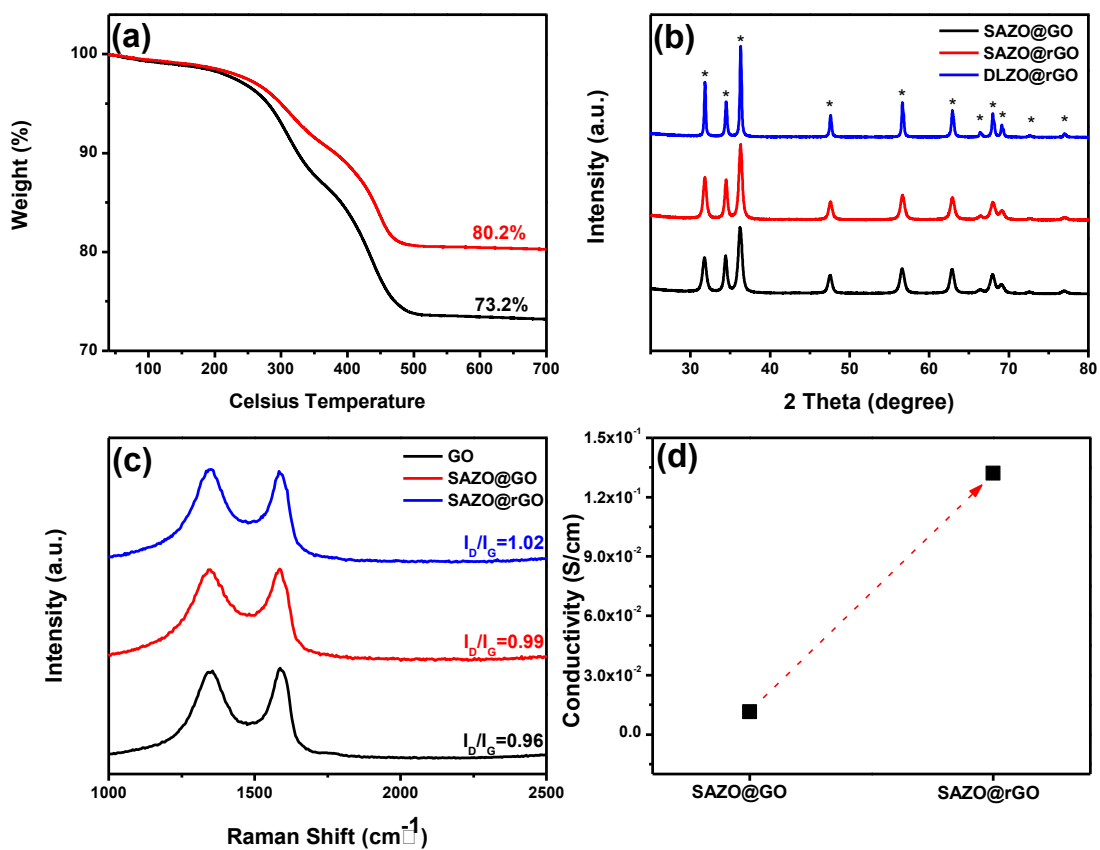


Figure 3.11 (a) TGA curves showing the temperature dependence of SAZO@GO synthesis; red line 125 °C, black line 95 °C. (b) XRD patterns of self-assembled ZnO and doughnut-like ZnO samples. (c) Raman spectra of GO and self-assembled ZnO with GO. (d) Electrical conductivity of SAZO@GO and SAZO@rGO.

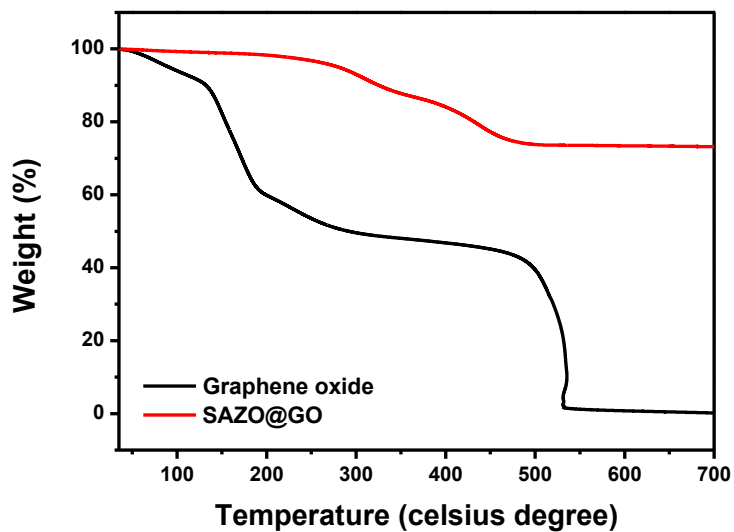


Figure 3.12 TGA curve of GO and SAZO@GO

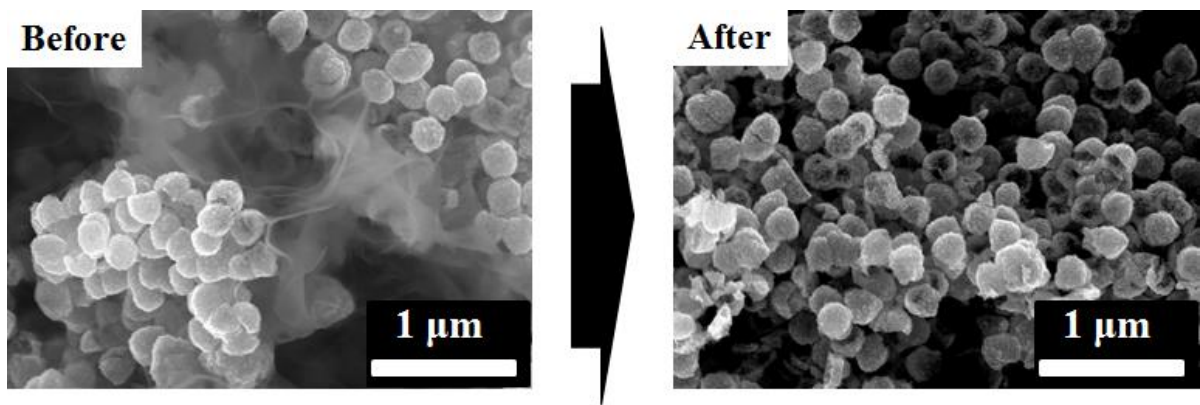


Figure 3.13 SEM images of SAZO@rGO before and after calcination under air atmosphere at 500 °C

3.3.5 Electrochemical measurement

Electrochemical measurements were performed using a 2032 coin-type half-cell, in which Li metal foil was used as the counter electrode. Figure 3.14a shows that the electrochemical behavior of the SAZO@rGO electrodes is characterized by CV at the scanning rate of 0.2 mV s^{-1} . The lithiation process of zinc oxide involves two separate reactions, conversion reaction and an alloying reaction. In the conversion reaction, zinc oxide is converted to zinc metal and amorphous Li_2O is generated. In the subsequent alloying reaction, the generated zinc metal can become Li_2Zn_5 , LiZn_2 , Li_2Zn_3 and LiZn by reacting with lithium ions.¹² In the first cathodic process, only a singular strong peak can be identified in the range of 0.5 - 0.1 V; this range is related to the reduction of ZnO to Zn at $> 0.3 \text{ V}$, the lithium-zinc alloy reaction at $< 0.3 \text{ V}$, and the formation of a gel-like SEI layer.^{12a} Although the potentials of these reactions are strictly speaking quite different, they are nonetheless very close and therefore present as just one strong peak. In the first anodic process, a number of peaks are observed at various voltages. Those peaks located at 0.35 V, 0.55 V, 0.68 V and 1.36 V are likely related to the de-alloying reactions of Li-Zn alloys^{12a, b}, while the weak peak at 2.35 V is indicative of the conversion reaction of Zn to ZnO . In subsequent cycles, the conversion reaction peak varies due to activation processes.

Figures 3.14b and 14c showed the cycling performance of the zinc oxides with rGO in range of 0.02-3.00 V (vs. Li^+/Li) at a current density of 100 mA g^{-1} . For comparison, galvanostatic discharge/charge experimental data for zinc oxide nanoparticle cluster (ZONC) and doughnut-like zinc oxide (DLZO) electrode without rGO under similar conditions are also presented. The first discharge capacity of all samples exceeds the theoretical value of 988 mAh g^{-1} , which is believed to be due to decomposition of the electrolyte upon reduction at low potential in the conversion reaction.¹³ The specific capacity of all electrodes, with rGO or without rGO, rapidly decreases during the initial cycling but rapidly rebounds after a certain number of cycles due to an as yet unidentified activation process.^{3b} After 65 cycles, the reversible discharge capacities of the SAZO@rGO and DLZO@rGO electrodes were 752.8 and 517.7 mAh g^{-1} , respectively, whereas the ZONC and DLZO electrodes without rGO showed disastrous performance. In the case of SAZO@rGO and DLZO@rGO electrodes, the rGO served to improve the electrical conductivity and leads to better retention; however, the insulating nature of ZONC and DLZO inhibits cycling retention and causes the capacity to fade after the initial 10 cycles. The initial coulombic efficiencies (CEs) of both SAZO@rGO and DLZO@rGO electrodes were very poor (51.0 and 65.7 %) due to decomposition of the electrolyte in the first cycle, the formation of a SEI layer, and an undetermined irreversible reaction; however, the CEs of both electrodes rapidly increased during the initial 10 cycles and eventually reached up to 99.1 %. The more rapid increase in CEs seen with the SAZO@rGO electrode means that it achieved faster stabilization and electrode activation than DLZO@rGO electrode. More importantly, the

cycling performance of zinc oxides with rGO in the 0.02-3.00 V range (vs. Li⁺/Li) at a current density of 500 mA g⁻¹ show a direct difference in the cyclic stability of both electrodes (Figure S11). In the case of the SAZO@rGO electrode for example, the discharge capacity is stabilized over a long number of cycles despite an initial decrease in capacity. Conversely, the cyclic capacity of the DLZO@rGO electrode decreased rapidly after 30 cycles and exhibited a particularly poor cyclic stability at a high current density (500 mA g⁻¹).

This phenomenon was also observed in the cycling performance of SAZO@rGO and DLZO@rGO electrodes at various current densities. After a rapid fading of capacity during the initial cycle at low current (100 mA g⁻¹) due to activation of the electrodes, the capacity remained stable during cycling at various current densities with all samples, though the SAZO@rGO electrode exhibited better reversible performance under all the conditions. The discharge capacities of the SAZO@rGO electrode were 631.2, 515.9, 404.4, and 259.7 mAh g⁻¹ at current densities of 250, 500, 1000 and 2000 mA g⁻¹, respectively, while for the DLZO@rGO electrode, these values were 449.8, 360.4, 267.8 and 190.0 mAh g⁻¹. When the current density reverted to 100 mA g⁻¹ during cycling, the reversible capacities of the SAZO@rGO and DLZO@rGO electrode were > 700 mAh g⁻¹ and, 400 mAh g⁻¹, respectively.

The reason for the higher and more stable performance of the SAZO@rGO electrode is attributable to benefits of a hierarchical self-assembled structure. Specifically, such a structure incorporates a void space that can act as a buffer to the intense volume expansion that occurs during cycling.^{3b} Furthermore, the SAZO@rGO electrode can form a stable SEI layer on its outer surface.^{3b} Figure 3.16 shows SEM images of SAZO@rGO and DLZO@rGO electrodes before and after cycling, in which the SAZO@rGO electrode clearly maintains its morphology after 100 cycles, whereas the DLZO@rGO electrode cannot maintain its doughnut-like structure.

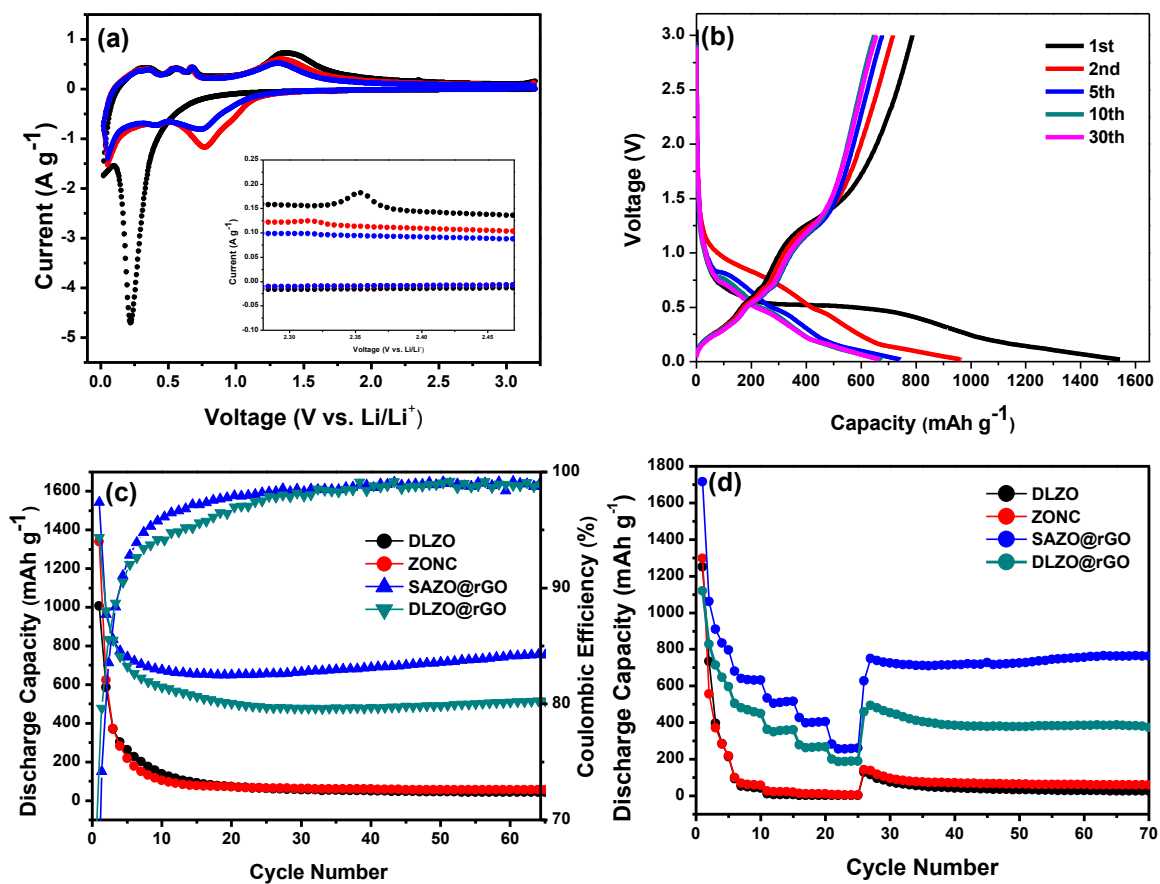


Figure 3.14 (a) Cyclic voltammograms of a SAZO@rGO electrode at a scanning rate of 0.2 mV s^{-1} . (b) Discharge-charge curves for SAZO@rGO. (c) Cycling performance of ZnO electrodes at a current density of 100 mA g^{-1} . (d) Rate performance of ZnO electrodes.

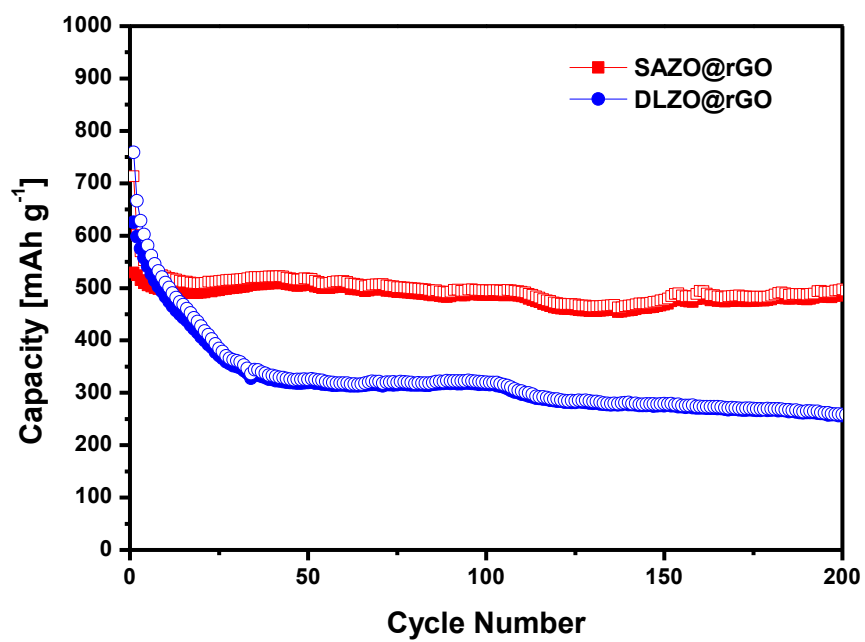


Figure 3.15 Cycling performance of ZnO electrodes at a current density of 500 mA g^{-1} .

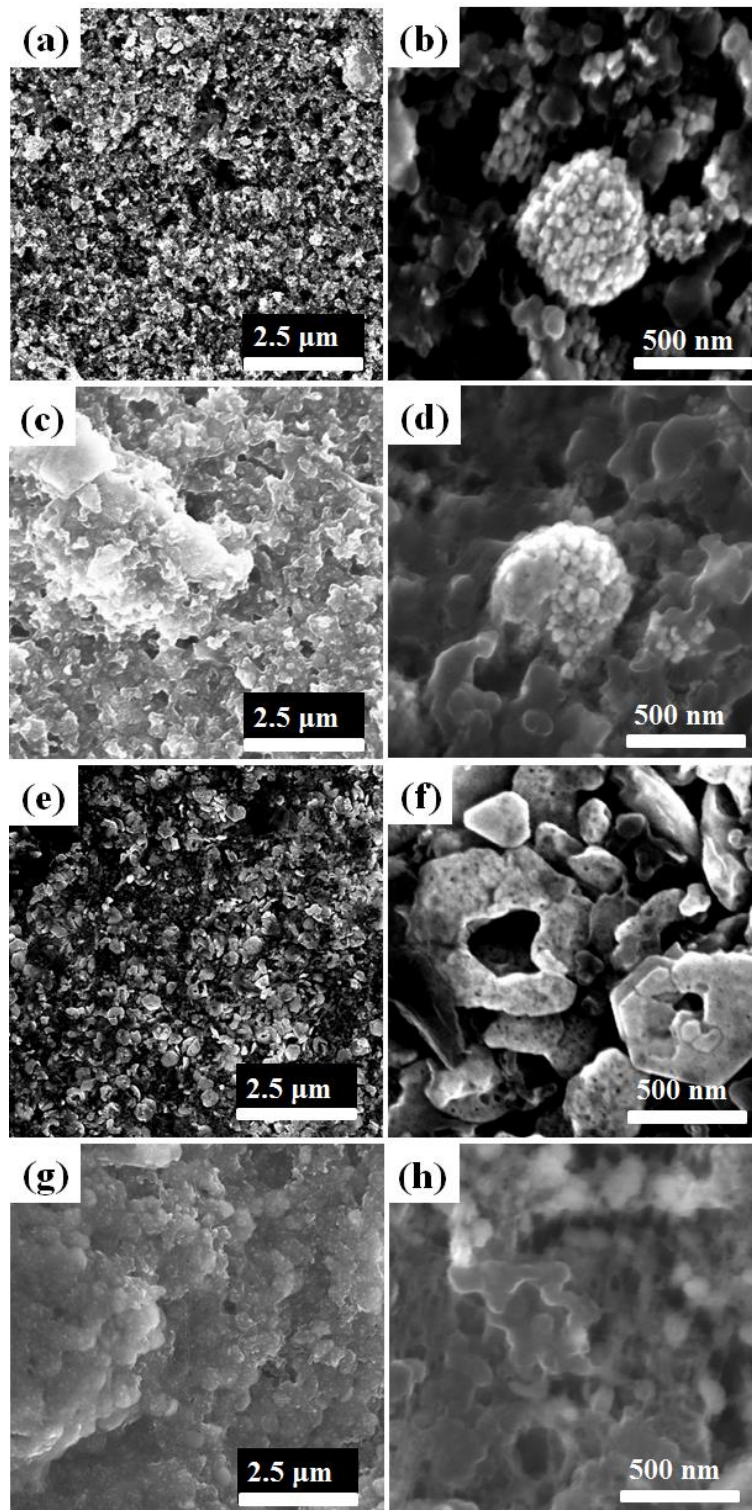


Figure 3.16 SEM images of SAZO@rGO and DLZO@rGO electrodes before and after cycling; SEM images of (a, b) bare SAZO@rGO electrode and (e, f) bare DLZO@rGO electrode. SEM images of (c, d) SAZO@rGO electrode and (g, h) bare DLZO@rGO electrode after 100cycles in condition of current density 500 mA g^{-1} .

3.4 Conclusions

A simple method for the hierarchical self-assembly of ZnO was successfully developed by using GO. Though the GO plays a leading role in creating the self-assembled structure, it also serves to overcome the electrically insulating nature of zinc oxide. As an anode in a lithium ion battery, the hierarchical structure exhibits excellent cycle stability, higher cycling performance and better rate capabilities than a doughnut-like ZnO structure. Furthermore, self-assembled ZnO with rGO offers advantages in terms of high electrical conductivity, short diffusion length, a stable SEI layer, and sufficient buffer space to accumulate the intense volume expansion during cycling.

3.5 Reference

1. Arico, A. S.; Bruce, P.; Scrosati, B.; Tarascon, J. M.; van Schalkwijk, W., Nanostructured materials for advanced energy conversion and storage devices. *Nature materials* **2005**, *4* (5), 366-77.
2. (a) Lee, S.; Cho, Y.; Song, H.-K.; Lee, K. T.; Cho, J., Carbon-Coated Single-Crystal LiMn_2O_4 Nanoparticle Clusters as Cathode Material for High-Energy and High-Power Lithium-Ion Batteries. *Angew. Chem. Int. Ed.* **2012**, *51*, 8748-8752; (b) Wang, H.; Cui, L.-F.; Yang, Y.; Casalongue, H. S.; Robinson, J. T.; Liang, Y.; Cui, Y.; Dai, H., Mn_3O_4 -Graphene Hybrid as a High-Capacity Anode Material for Lithium Ion Batteries. *Journal of the American Chemical Society* **2010**, *132*, 13978-13980; (c) Wang, J.; Sun, X., Understanding and recent development of carbon coating on LiFePO_4 cathode materials for lithium-ion batteries. *Energy Environ. Sci.* **2012**, *5*, 5163-5185; (d) Liu, J.; Xue, D., Hollow Nanostructured Anode Materials for Li-Ion Batteries. *Nanoscale research letters* **2010**, *5* (10), 1525-1534; (e) Wang, Y.; Wang, Y.; Hosono, E.; Wang, K.; Zhou, H., The Design of a LiFePO_4 /Carbon Nanocomposite With a Core-Shell Structure and Its Synthesis by an In Situ Polymerization Restriction Method. *Angew. Chem. Int. Ed.* **2008**, *47* (39), 7461-7465.
3. (a) Lu, Y.; Tu, J. P.; Xiang, J. Y.; Wang, X. L.; Zhang, J.; Mai, Y. J.; Mao, S. X., Improved Electrochemical Performance of Self-Assembled Hierarchical Nanostructured Nickel Phosphide as a Negative Electrode for Lithium Ion Batteries. *J. Phys. Chem. C* **2011**, *115*, 23760-23767; (b) Lee, S. H.; Yu, S.-H.; Lee, J. E.; Jin, A.; Lee, D. J.; Lee, N.; Jo, H.; Shin, K.; Ahn, T.-Y.; Kim, Y.-W.; Choe, H.; Sung, Y.-E.; Hyeon, T., Self-Assembled Fe_3O_4 Nanoparticle Clusters as High-Performance Anodes for Lithium Ion Batteries via Geometric Confinement. *Nano letters* **2013**, *13*, 4249-4256; (c) Lee, J. E.; Yu, S.-H.; Lee, D. J.; Lee, D.-C.; Han, S. I.; Sung, Y.-E.; Hyeon, T., Facile and economical synthesis of hierarchical carbon-coated magnetite nanocomposite particles and their applications in lithium ion battery anodes. *Energy Environ. Sci.* **2012**, *5*, 9528-9533; (d) A. Magasinski; P. Dixon; B. Hertzberg; A. Kvit; Ayala, J.; Yushin, G., High-performance lithium-ion anodes using a hierarchical bottom-up approach. *Nat. Mater.* **2010**, *9*, 353-358.
4. (a) Jang, B.; Park, M.; Chae, O. B.; Park, S.; Kim, Y.; Oh, S. M.; Piao, Y.; Hyeon, T., Direct Synthesis of Self-Assembled Ferrite/Carbon Hybrid Nanosheets for High Performance Lithium-Ion Battery Anodes. *Journal of the American Chemical Society* **2012**, *134*, 15010-15015; (b) Oh, S. W.; Myung, S.-T.; Oh, S.-M.; Oh, K. H.; Amine, K.; Scrosati, B.; Sun, Y.-K., Double Carbon Coating of LiFePO_4 as High Rate Electrode for Rechargeable Lithium Batteries. *Adv. Mater.* **2010**, *22*, 4842-4845.
5. (a) Xu, X.; Cao, R.; Jeong, S.; Cho, J., Spindle-like Mesoporous $\alpha\text{-Fe}_2\text{O}_3$ Anode Material Prepared from MOF Template for High-Rate Lithium Batteries. *Nano letters* **2012**, *12*, 4988-4991; (b) Sun, Y.; Hu, X.; Luo, W.; Huang, Y., Self-assembled hierarchical MoO_2 /graphene nanoarchitectures and their application as a high-performance anode material for lithium-ion batteries. *ACS nano* **2011**, *5* (9), 7100-7; (c) Shuangling Jin; Honggui Deng; Donghui Long; Xiaojun Liu; Liang Zhan; Xiaoyi Liang; Wenming Qiao; Ling, L., Facile synthesis of hierarchically structured Fe_3O_4 /carbon micro-flowers and their application to lithium-ion battery anodes. *journal of Power Sources* **2011**, *196*, 3887-3893; (d) Yang, H.; Wu, X.-L.; Cao, M.-H.; Guo, Y.-G., Solvothermal Synthesis of LiFePO_4 Hierarchically Dumbbell-Like Microstructures by Nanoplate Self-Assembly and Their Application as a Cathode Material in Lithium-Ion Batteries. *J. Phys. Chem. C* **2009**, *113* (8), 3345-

- 3351; (e) Demir-Cakan, R.; Hu, Y.-S.; Antonietti, M.; Maier, J.; Titirici, M.-M., Facile One-Pot Synthesis of Mesoporous SnO₂ Microspheres via Nanoparticles Assembly and Lithium Storage Properties. *Chem. Mater.* **2008**, *20* (4), 1227-1229; (f) Lin, Y.-S.; Tsai, M.-C.; Duh, J.-G., Self-assembled synthesis of nanoflower-like Li₄Ti₅O₁₂ for ultrahigh rate lithium-ion batteries. *Journal of Power Sources* **2012**, *214*, 314-318.
6. Marcano, D. C.; Kosynkin, D. V.; Berlin, J. M.; Sinitskii, A.; Sun, Z.; Slesarev, A.; Alemany, L. B.; Lu, W.; Tour, J. M., Improved synthesis of graphene oxide. *ACS nano* **2010**, *4* (8), 4806-14.
 7. Rodríguez-Gattorno, G.; Santiago-Jacinto, P.; Rendon-Vázquez, L.; Németh, J.; Dékány, I.; D'áz, D., Novel Synthesis Pathway of ZnO Nanoparticles from the Spontaneous Hydrolysis of Zinc Carboxylate Salts. *J. phys. Chem. B* **2003**, *107*, 12597-12604.
 8. Son, D. I.; Kwon, B. W.; Park, D. H.; Seo, W.-S.; Yi, Y.; Angadi, B.; Lee, C.-L.; Choi, W. K., Emissive ZnO-graphene quantum dots for white-light-emitting diodes. *Nature nanotechnology* **2012**, *7*, 465-471.
 9. (a) Yu, S.-H.; Conte, D. E.; Baek, S.; Lee, D.-C.; Park, S.-K.; Lee, K. J.; Piao, Y.; Sung, Y.-E.; Pinna, N., Structure-Properties Relationship in Iron Oxide-Reduced Graphene Oxide Nanostructures for Li-Ion Batteries. *Adv. Funct. Mater.* **2013**; (b) Wang, H.; Yang, Y.; Liang, Y.; Cui, L. F.; Casalongue, H. S.; Li, Y.; Hong, G.; Cui, Y.; Dai, H., LiMn_(1-x)Fe_(x)PO₄ nanorods grown on graphene sheets for ultrahigh-rate-performance lithium ion batteries. *Angewandte Chemie* **2011**, *50* (32), 7364-8; (c) Zhu, X.; Zhu, Y.; Murali, S.; Stoller, M. D.; Ruoff, R. S., Nanostructured reduced graphene oxide/Fe₂O₃ composite as a high-performance anode material for lithium ion batteries. *ACS nano* **2011**, *5* (4), 3333-8.
 10. Yang, S.; Feng, X.; Ivanovici, S.; Mullen, K., Fabrication of Graphene-Encapsulated Oxide Nanoparticles: Towards High-Performance Anode Materials for Lithium Storage. *Angew. Chem. Int. Ed.* **2010**, *49*, 8408-8411.
 11. Jung, Y. S.; Cavanagh, A. S.; Dillon, A. C.; Groner, M. D.; George, S. M.; Lee, S.-H., Enhanced Stability of LiCoO₂ Cathodes in Lithium-Ion Batteries Using Surface Modification by Atomic Layer Deposition. *Journal of The Electrochemical Society* **2010**, *157* (1), A75-A81.
 12. (a) Chae, O. B.; Park, S.; Ryu, J. H.; Oh, S. M., Performance Improvement of Nano-Sized Zinc Oxide Electrode by Embedding in Carbon Matrix for Lithium-Ion Batteries. *Journal of The Electrochemical Society* **2013**, *160* (1), A11-A14; (b) Huang, X. H.; Xia, X. H.; Yuan, Y. F.; Zhou, F., Porous ZnO nanosheets grown on copper substrates as anodes for lithium ion batteries. *Electrochimica Acta* **2011**, *56* (14), 4960-4965; (c) Zhang, C. Q.; Tu, J. P.; Yuan, Y. F.; Huang, X. H.; Chen, X. T.; Mao, F., Electrochemical Performances of Ni-Coated ZnO as an Anode Material for Lithium-Ion Batteries. *Journal of The Electrochemical Society* **2007**, *154* (2), A65-A69.
 13. (a) Cabana, J.; Monconduit, L.; Larcher, D.; Palacín, M. R., Beyond Intercalation-Based Li-Ion Batteries: The State of the Art and Challenges of Electrode Materials Reacting Through Conversion Reactions. *Adv. Energy Mater.* **2010**, *22*, E170-E192; (b) Ponrouch, A.; Taberna, P.-L.; Simon, P.; Palacín, M. R., On the origin of the extra capacity at low potential in materials for Li batteries reacting through conversion reaction. *Electrochimica Acta* **2012**, *61*, 13-18.